Temperature and magnetic field limits of a kinetic inductance traveling-wave parametric amplifier

Lucas M. Janssen,[1] Farzad Faramarzi,[2] Henry G. LeDuc,[2] Sahil Patel,[2,3] Gianluigi Catelani,[4,5] Peter K. Day,[2] Yoichi Ando,[1,*] and Christian Dickel[1,†]

[1] *Physics Institute II, University of Cologne, Zülpicher Str. 77, 50937 Köln, Germany*
[2] *Jet Propulsion Laboratory, California Institute of Technology, Pasadena, California 91101, USA*
[3] *Department of Applied Physics and Materials Science, California Institute of Technology, Pasadena, California 91125, USA*
[4] *Institute for Theoretical Nanoelectronics (PGI-2), Forschungszentrum Jülich, 52428 Jülich, Germany*
[5] *Quantum Research Center, Technology Innovation Institute, Abu Dhabi 9639, UAE*

(Received 19 September 2025; revised 26 February 2026; accepted 13 May 2026; published 15 June 2026)

Kinetic inductance traveling-wave parametric amplifiers (KI-TWPAs) offer broadband near-quantum-limited amplification with high saturation power. Because of the high critical magnetic fields of high-kinetic inductance, KI-TWPAs should be resilient to magnetic fields. In this work, we study how magnetic field and temperature affect the performance of a KI-TWPA based on a thin-NbTiN inverse microstrip with a Nb ground plane. This KI-TWPA can provide substantial signal-to-noise-ratio improvement (ΔSNR) up to in-plane magnetic fields of 0.35 T and out-of-plane fields of 50 mT, considerably higher than what has been demonstrated with TWPAs based on Josephson junctions. The field compatibility can be further improved by incorporating vortex traps and by using materials with higher critical fields. We also find that the gain does not degrade when the temperature is raised to 3 K (limited by the Nb ground plane), while ΔSNR decreases with temperature, consistent with expectations. This demonstrates that KI-TWPAs can be used in experiments that need to be performed at relatively high temperatures. The operability of KI-TWPAs in high magnetic fields opens the door to a wide range of applications in spin qubits, spin ensembles, topological qubits, low-power NMR, and the search for axion dark matter.

DOI: 10.1103/pp6n-9vzj

I. INTRODUCTION

Kinetic inductance traveling-wave parametric amplifiers (KI-TWPAs) [1] have emerged as promising technology that can offer large instantaneous bandwidth, high dynamic range, and near-quantum-limited added noise [2–5]. They are already becoming established for the readout of arrays of energy-resolving single-photon-counting superconducting detectors, such as microwave kinetic inductance detectors [6,7] and transition edge sensors [8]. The low added noise makes them, in principle, suitable for superconducting qubit readout [9], but the higher pump powers compared to those of Josephson TWPAs (J-TWPAs) may present practical challenges.

Although J-TWPAs have undergone substantial development [10–14], KI-TWPAs offer four distinct advantages: higher saturation power, magnetic field resilience, higher-temperature operation and higher-frequency operation. The resilience of KI-TWPAs to magnetic fields can be attributed to two factors: the inherently high critical fields of high-kinetic-inductance materials (e.g., NbTiN or TiN, as opposed to predominantly aluminum-based Josephson junctions) and the absence of the Fraunhofer effect, which in Josephson junctions can cause oscillatory suppression of the critical current at millitesla-scale fields [15]. SQUID-based J-TWPAs [12,14] are often sensitive to submillitesla out-of-plane fields. The impressive field resilience of kinetic inductance materials has already been shown in recent works on cavity-based kinetic inductance parametric amplifiers [16–21]; however, these amplifiers suffer from lower bandwidths and saturation power compared to KI-TWPAs because of their resonant nature.

There is already a growing number of experiments that employ TWPAs and require relatively high magnetic fields at the samples [22–28]. In addition, there are many examples of experiments that would benefit from a TWPA, e.g., in superconducting qubits [29–35], quantum dots and spin qubits [26,36–38], spin ensembles or low-power NMR [23,39,40], topological qubits [27,28], as well as hybrid setups including mechanical [41,42] and magnonic degrees

*Contact author: ando@ph2.uni-koeln.de
†Contact author: dickel@ph2.uni-koeln.de

of freedom [43,44], and the search for axion dark matter [24,25,45,46].

KI-TWPAs based on NbTiN can also operate at higher temperatures because of the high critical temperature of NbTiN, making them more versatile. In the future, they might replace commonly used cryogenic HEMT amplifiers in some use cases, with similar performance at a fraction of the power dissipation [47].

Here, we characterize the performance of a KI-TWPA, with NbTiN as the microstrip layer and Nb as the ground layer, as a function of temperature and different magnetic field directions. We measure both gain and signal-to-noise-ratio (SNR) improvement, ΔSNR, which quantifies the improvement over the subsequent amplification chain. We find that the KI-TWPA maintains a significant improvement in SNR (>3 dB) up to 1.2 K, although higher temperatures increase the idler noise because the input port of the device is terminated at the variable-temperature stage. The temperature dependence of the unpumped transmission of the TWPA can be modeled using Mattis-Bardeen theory with temperature-dependent suppression of the superconducting gap. Similarly, ΔSNR can be modeled by assuming an ideal four-wave-mixing parametric amplifier cascaded with a second amplifier, demonstrating near-quantum-limited noise.

We next study the effect of magnetic fields, both in-plane and perpendicular. We report an order-of-magnitude improvement in field resilience over J-TWPAs in the bottleneck field directions. Critically, ΔSNR measurements reveal that practical amplifier performance can degrade before gain degradation becomes apparent, emphasizing the importance of measuring both metrics. The magnetic field dependence shows behavior that cannot be explained simply in terms of gap suppression by the field. In fact, considerable hysteresis with the magnetic field indicates that vortex dynamics in the niobium ground plane, but likely also in the narrow center conductor, play a dominant role. While we do not develop a quantitative model that includes vortex dynamics, the measured performance thresholds provide clear operational guidelines. With the demonstrated field resilience, KI-TWPAs can be incorporated into most experimental setups in which the amplifier can be mounted at some distance from the magnet [15], especially when stray fields are predominantly in-plane.

II. EXPERIMENTAL DETAILS

An optical image of the TWPA chip is shown in Fig. 1(b), with an enlarged view showing the inverse microstrip with modulated capacitive stubs [Fig. 1(c)]. The device design is identical to that presented in Ref. [3]. In summary, the device is a kinetic inductance photonic crystal TWPA in an inverted microstrip geometry. The transmission line is a thin film of NbTiN with protruding capacitive stubs. The length of the capacitive stubs is periodically modulated to introduce a bandgap in the device transmission around 12 GHz. The device ground plane is a 200-nm-thick niobium film. We operate the TWPA in the four-wave-mixing mode by injecting pump frequencies

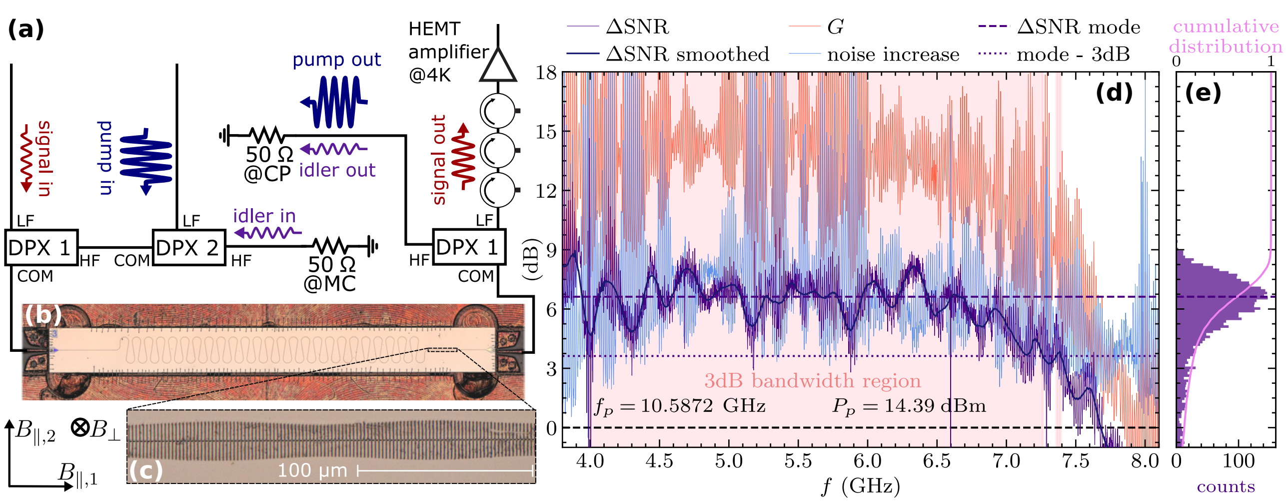

FIG. 1. (a) Measurement setup with diplexers for coupling the pump tone in and out and for idler thermalization. After the TWPA, there are circulators and a HEMT amplifier in the cryogenic signal chain. (b) Microscope image of the TWPA showing a meandering microstrip. Magnetic field directions $B_{\perp}$, $B_{\parallel,1}$, and $B_{\parallel,2}$ are related to the device geometry. (c) Enlarged view of the microstrip region showing the capacitive-loading stubs with modulated length for bandgap engineering. (d) Representative SNR-improvement ΔSNR and gain G curves for the indicated pump settings at zero field and base temperature. Here ΔSNR is the difference between gain and added noise. The shaded region indicates the 3-dB bandwidth, where the (slightly smoothed) ΔSNR exceeds the ΔSNR mode minus 3 dB. (e) Histogram of all ΔSNR values (bar plot) and smoothed cumulative distribution (pink line plot). The ΔSNR mode is defined as the point of maximum slope of the smoothed cumulative distribution. The mode is used as a robust way to estimate a noisy plateau value.

below the bandgap. Magnetic field directions relative to the TWPA chip are also indicated in Fig. 1. A more detailed description of the device is provided in Appendix A. In the main text, we focus on the out-of-plane direction, $B_\perp$, and the in-plane direction along the long axis of the chip, $B_{\parallel,1}$, data for $B_{\parallel,2}$ can be found in Appendix E 2.

Using a combination of diplexers (DPX1 and DPX2) before the TWPA, we supply the pump tone and signal tones to the device. Additionally, we provide a cold termination ($T < \hbar\omega_{\mathrm{idler}}/k_B$) at the input of the device over the idler band to keep the device quantum limited. Using a third diplexer, identical to DPX1, at the output of the device, we terminate the idler frequencies and the pump tone at a higher dilution-refrigerator stage to reduce the heat load on the mixing chamber and to prevent the following amplifiers from saturating. This pump-output and idler-output termination should help reduce the added noise of the amplifier, even if we cannot terminate it at the mixing-chamber temperature because of cooling-power limitations. Coupling out the TWPA pump tone from the signal line is also important, as it would otherwise saturate the subsequent amplifiers. Given high attenuation on the input line, we could not straightforwardly measure the saturation power of the TWPA in this setup. However, previous measurements of a similar device showed a 1-dB gain compression with 15 dB of gain at an input power of −58 dBm [3]. A more detailed description of the measurement setup is provided in Appendix A.

In the following, we need figures of merit for the amplifier performance to characterize the temperature and field dependence. We focus on the insertion loss, the true gain, the SNR improvement, and the bandwidth. The way we define and calculate these figures of merit from the data is illustrated in Figs. 1(d) and 1(e). Calibration measurements with a short cable in place of the TWPA provide a reference for calculating the true gain and added noise from the measured S_{21} and noise spectrum. True gain is the net signal amplification relative to this bypass connection, inherently accounting for the device insertion loss. We calculate ΔSNR as the difference between gain and added noise. Crucially, we optimize the pump power P_p and frequency f_p by maximizing the mean ΔSNR in the 4–8-GHz band, $\langle \Delta\mathrm{SNR}\rangle_{4-8\,\mathrm{GHz}}$ (for data on the pump optimization, see Appendix B). For the field and temperature dependence, we optimize the pump settings at every temperature or magnetic field. We then extract the typical value of $\Delta\mathrm{SNR}(f)$ by approximating the ΔSNR mode—the most commonly occurring value. Figure 1(e) shows a measured-data histogram and cumulative probability distribution. Relative to the ΔSNR mode, we define the 3-dB-bandwidth $\mathrm{BW}_{3\,\mathrm{dB}}$ by smoothing the ΔSNR data and finding ranges of frequencies where ΔSNR exceeds the mode value minus 3 dB. The bandwidth regions need not be continuous; when referring to $\mathrm{BW}_{3\,\mathrm{dB}}$ in frequency units, we sum the disjoint frequency regions. However, the bandwidth is typically continuous for the optimized pump settings. All quoted bandwidths are based on ΔSNR, not on the gain profiles. We then show the mean values of ΔSNR and true gain within the bandwidth: $\langle\Delta\mathrm{SNR}\rangle_{\mathrm{BW}}$ and $\langle G\rangle_{\mathrm{BW}}$. The error bars in the plots below represent the 25th and 75th percentiles of the data within the bandwidth.

III. TEMPERATURE DEPENDENCE

We begin by discussing the KI-TWPA temperature dependence and the model that describes TWPA S_{21} as a function of T; the model provides insight into the underlying physics and will help us better understand the magnetic field dependence. Figure 2(a) shows $\langle \mathrm{TWPA}\, S_{21}\rangle_{4-8\,\mathrm{GHz}}$, the transmission calibrated against a bypass cable, as a

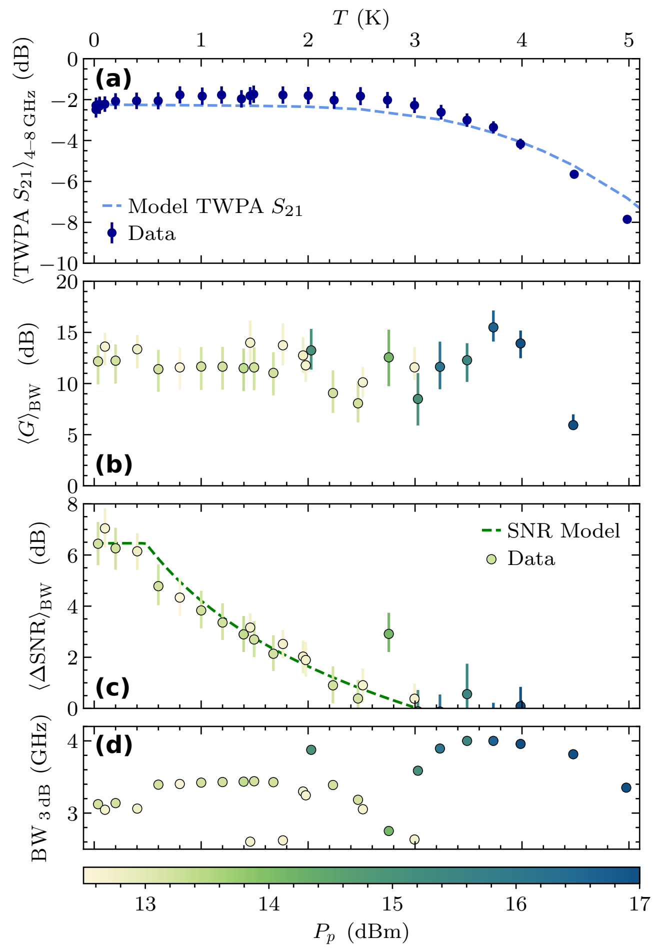

FIG. 2. (a) $\langle \mathrm{TWPA}\, S_{21}\rangle_{4-8\,\mathrm{GHz}}$ versus temperature T showing a plateau up to about 3 K. (b) True gain within the bandwidth, $\langle G\rangle_{\mathrm{BW}}$, versus T, showing a plateau up to 4 K. Around 3 K, the P_p (optimized at every temperature) increases, likely compensating for the increased insertion loss. (c) $\langle\Delta\mathrm{SNR}\rangle_{\mathrm{BW}}$ versus T, showing a decrease in line with a model based on an ideal four-wave-mixing parametric amplifier with input noise. Above $T = 2.5$ K, it drops below 0 dB. (d) $\mathrm{BW}_{3\,\mathrm{dB}}$ versus T. Bandwidth increases when optimized P_p increases at high T and then drops.

function of temperature T. There is no significant change in the transmission of the device up to 3 K. Here we show only the $\langle \text{TWPA}\, S_{21}\rangle_{4-8\,\text{GHz}}$ data for a reduced temperature range, where the TWPA still provides gain; the full dependence on frequency and temperature can be found in Appendix C.

We modeled the temperature dependence using Mattis-Bardeen theory of ac conductivity [48], taking into account the temperature dependence of the gap (Appendix D), and found qualitative agreement. The surface impedance of both superconductors (Nb and NbTiN) is calculated using this model, which reveals that changes in the ground-plane surface resistance as a function of temperature dominate the change in $\langle \text{TWPA}\, S_{21}\rangle_{4-8\,\text{GHz}}$. Thus, a fully NbTiN-based device would likely operate beyond 4 K with minimal loss.

Now we turn from the insertion loss to the TWPA performance based on the aforementioned figures of merit. Figures 2(b) and 2(c) show $\langle G\rangle_{\text{BW}}$ and $\langle \Delta\text{SNR}\rangle_{\text{BW}}$ versus T. The gain maintains similar values up to 4 K, but the optimized P_p starts to increase around 3 K, consistent with the increasing insertion loss. The bandwidth initially shows a slight increase and then increases further when the optimal P_p increases at high T.

We can model the temperature-dependent ΔSNR of the parametric amplifier cascaded with a second amplifier to check whether it is consistent with expectations and to estimate the TWPA added noise. In this case, the second amplifier is the HEMT amplifier shown in Fig. 1. Additional noise of the room-temperature amplifier should be negligible because of the high gain of the TWPA and the HEMT amplifier. In this experiment, we vary the temperature of the mixing chamber, where the signal and idler inputs of the TWPA are thermalized. The HEMT is thermalized at the 4 K stage. Its temperature stays approximately constant during the temperature sweep; thus, we assume a constant noise temperature. The parametric amplifier provides a true gain G, which is measured. We can estimate the temperature dependence of the added noise from the signal and idler ports at frequencies given by $2f_p = f_{\text{signal}} + f_{\text{idler}}$. The added-noise temperature at the signal and idler bands is given by $T_{\text{signal}} = (\hbar\omega_{\text{signal}}/k_B)(1 + 2n(\omega_{\text{signal}}, T_{\text{eff}}))$ and $T_{\text{idler}} = (\hbar\omega_{\text{idler}}/k_B)(1 + 2n(\omega_{\text{idler}}, T_{\text{eff}}))$, where $n(\omega, T_{\text{eff}})$ is the Bose-Einstein occupation number and $T_{\text{eff}} = \max(T, T_{\min})$ includes a minimum-noise floor $T_{\min}$ to account for the low-temperature plateau in ΔSNR [see Fig. 2(b)]. Using Friis's formula [49] for cascaded amplifiers, the total parametric amplifier noise temperature $T_p = T_{\text{signal}} + T_{\text{idler}}$ gives an SNR improvement

$$\Delta\text{SNR}_{\text{dB}} = 10\log_{10}\left(\frac{1}{T_p/T_{\text{2nd}} + 1/G_{\text{linear}}}\right). \qquad (1)$$

Fixing the TWPA gain at 12 dB, close to the measured values, we can fit this model to the data and find good agreement [see Fig. 2(c)]. The fit yields a second-amplifier noise temperature of $T_{\text{2nd}} = (12.9 \pm 0.3)$ K and $T_{\min} = (0.48 \pm 0.05)$ K. For the TWPA, $T_{\min}$ corresponds to approximately 1.7 added-noise photons at 6 GHz, which is in the expected range for a KI-TWPA [3]. The 13 K noise temperature of the second-stage amplifier exceeds the specified noise temperature of 3 K for the HEMT. This elevated noise temperature was also confirmed by a y-factor measurement of the setup without the TWPA, where we varied the mixing-chamber temperature and thus the HEMT input temperature. Using the Friis formula for lossy cascaded systems, approximately 3.9 dB of loss at 4 K would increase the effective noise temperature from 3 to 13 K. The specified total insertion loss of the diplexer plus circulators would be around 1.6 dB. Additionally, there are eight SMA connectors between the sample and HEMT, which could account for another 1.6 dB of loss. The amount of loss needed to explain the noise temperature would be at the high end of what we expect, especially given that the diplexers and circulators are nominally thermalized to the mixing-chamber stage. It is also possible that the HEMT is biased slightly suboptimally. Likely a combination of these effects leads to the elevated noise temperature we estimate for the HEMT.

IV. IN-PLANE MAGNETIC FIELD DEPENDENCE

The in-plane magnetic field dependence of the TWPA is shown in Fig. 3. Figure 3(a) shows $\langle \text{TWPA}\, S_{21}\rangle_{4-8\,\text{GHz}}$ versus $B_{\parallel,1}$, color coded by sweep direction to reveal hysteresis. For in-plane fields, the device insertion loss recovers its initial value when scanning back to zero field. Wider-range scans and detailed insertion-loss data are presented in Appendix E, showing that TWPA S_{21} is fully suppressed around 1.5 T, close to the critical field B_c of niobium (cf. Fig. 11 in Appendix F). Data for the $B_{\parallel,2}$ direction show less pronounced suppression and hysteresis, indicating possible magnet-to-sample misalignment, as it is not obvious that the two directions should differ based on the sample geometry.

The Mattis-Bardeen model that describes temperature dependence can be modified to include field-dependent gap suppression; however, it does not adequately describe the in-plane field dependence of TWPA S_{21}. Simple gap suppression with field would predict only an abrupt change near B_c, whereas we observe gradual degradation at much lower fields. Still, the model qualitatively reveals some of the effects that the field has on the device. In the model, the surface inductance changes by roughly an order of magnitude, both with temperature and magnetic field, but inductance changes do not dominate the TWPA S_{21} suppression. Moreover, unlike temperature, magnetic-field-induced gap

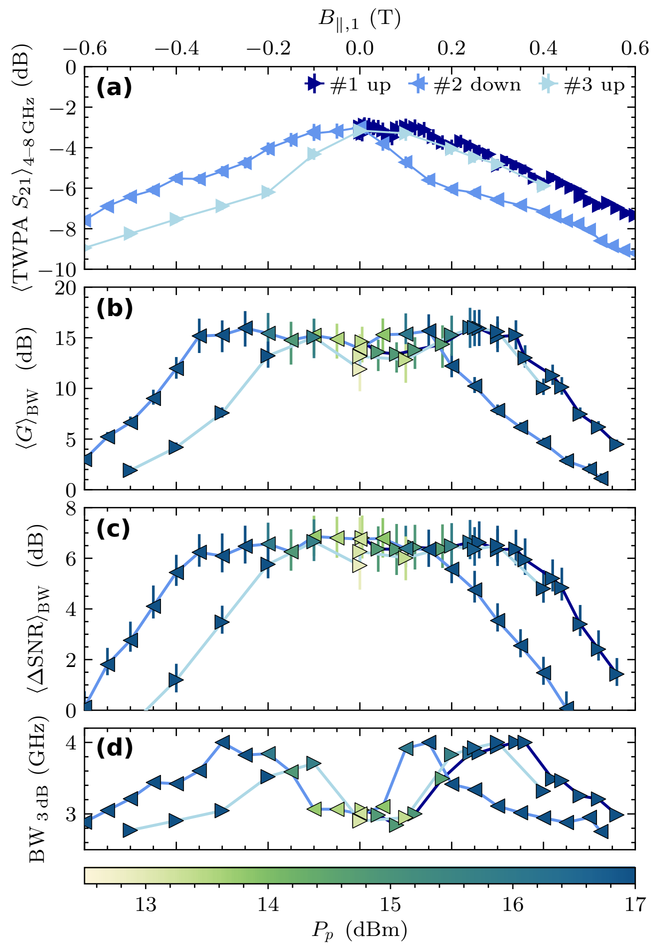

FIG. 3. (a) The $B_{\parallel,1}$ dependence of TWPA S_{21}. The sweep direction is color coded to reveal the hysteresis. (b) Corresponding gain curves at different $B_{\parallel,1}$. Pump settings are optimized at every field; data are selected for optimum $\langle\Delta\mathrm{SNR}\rangle_{4-8\,\mathrm{GHz}}$. Data points are color coded for P_p, and lines indicate sweep direction: higher $B_{\parallel,1}$ requires higher P_p, consistent with increased insertion loss. The hysteresis is also visible in the gain curves. (c) $\langle\Delta\mathrm{SNR}\rangle_{\mathrm{BW}}$ versus $B_{\parallel,1}$, following the gain curves. (d) $\mathrm{BW}_{3\,\mathrm{dB}}$ at different $B_{\parallel,1}$, showing an initial increase and then a decrease. $\mathrm{BW}_{3\,\mathrm{dB}}$ is maximized at $B_{\parallel,1} \approx 0.2$ T, while gain and $\langle\Delta\mathrm{SNR}\rangle_{\mathrm{BW}}$ remain similar to their zero-field values. $\mathrm{BW}_{3\,\mathrm{dB}}$ shows clear hysteresis.

suppression alone does not increase surface resistance (except near B_c).

Two effects can explain the additional change in surface resistance observed in the experiment: the presence of vortices and their motion in the niobium ground plane (partly due to field misalignment), or screening currents from flux penetration that enhance pair breaking. Advanced models that account for vortices can describe field dependence in superconducting resonators [50], and field-dependent gap changes could help constrain parameters, as in Ref. [15]. The reasonable agreement for the temperature dependence suggests that the modeling approach is sound, but it requires better niobium ground-plane impedance modeling. However, unknown misalignment complicates this, since $B_\perp$ and $B_\parallel$ dependencies differ significantly. We therefore focus on measured performance thresholds rather than pursuing quantitative modeling of the magnetic field dependence.

Figure 3(b) shows the corresponding gain curves at different $B_{\parallel,1}$ values. The gain is optimized at every field value, and the plotted data are selected for optimum $\langle\Delta\mathrm{SNR}\rangle_{4-8\,\mathrm{GHz}}$. Data points are color coded for P_p, revealing that, in general, higher $B_{\parallel,1}$ requires higher P_p, in line with the increased insertion loss. Figure 3(c) shows $\langle\Delta\mathrm{SNR}\rangle_{\mathrm{BW}}$ as a function of $B_{\parallel,1}$, which follows the gain curves. Figure 3(d) shows $\mathrm{BW}_{3\,\mathrm{dB}}$ at different $B_{\parallel,1}$ values, showing an initial increase with field followed by a decrease. At $B_{\parallel,1} \approx 0.3$ T, $\mathrm{BW}_{3\,\mathrm{dB}}$ is maximized, while the gain and $\langle\Delta\mathrm{SNR}\rangle_{\mathrm{BW}}$ remain similar to their zero-field values. The increased bandwidth likely results from field-induced losses suppressing internal reflections and impedance mismatches within the TWPA. Because the KI-TWPA experiences small but finite reflections at its terminations, the high parametric gain leads to cavity-like standing-wave structure in the gain spectrum, which limits the contiguous "usable" bandwidth. Additional internal loss reduces the effective loop gain of these unintended resonances, thereby suppressing the gain ripples they produce. This reduction in cavity finesse broadens and flattens the gain profile, so the measured bandwidth (defined by a minimum gain and maximum ripple) increases slightly despite the lower overall gain. Given that the net gain $\langle G\rangle_{\mathrm{BW}}$ and $\langle\Delta\mathrm{SNR}\rangle_{\mathrm{BW}}$ remain similar and the bandwidth increases, while $\langle\mathrm{TWPA}\,S_{21}\rangle_{4-8\,\mathrm{GHz}}$ slightly decreases, these losses are evidently compensated. The $\mathrm{BW}_{3\,\mathrm{dB}}$ shows clear hysteresis correlated with the changed insertion loss (likely correlating with the larger optimum P_p).

V. OUT-OF-PLANE MAGNETIC FIELD DEPENDENCE

The out-of-plane magnetic field dependence of the TWPA is shown in Fig. 4. Figure 4(a) shows the $B_\perp$ dependence of $\langle\mathrm{TWPA}\,S_{21}\rangle_{4-8\,\mathrm{GHz}}$. The hysteresis is much more pronounced than for $B_{\parallel,1}$. The TWPA S_{21} for a wider field range can be found in Appendix E. Overall, this hysteresis is similar to what has been observed in superconducting resonators [51]. It appears that after scanning to high $B_\perp$, the initial TWPA S_{21} is not fully recovered, but the transmission does recover when scanning slightly past zero field. We have dc measurements of B_c along the $B_\perp$ axis for a film similar to the niobium ground plane (Appendix F); we estimate B_c to be in the range 1.5–1.9 T, much larger than the fields at which transmission is suppressed here. This, combined with the pronounced hysteresis, indicates that the dominant physics is due to vortices rather than gap suppression. While theoretical frameworks exist for modeling field-dependent superconductor losses

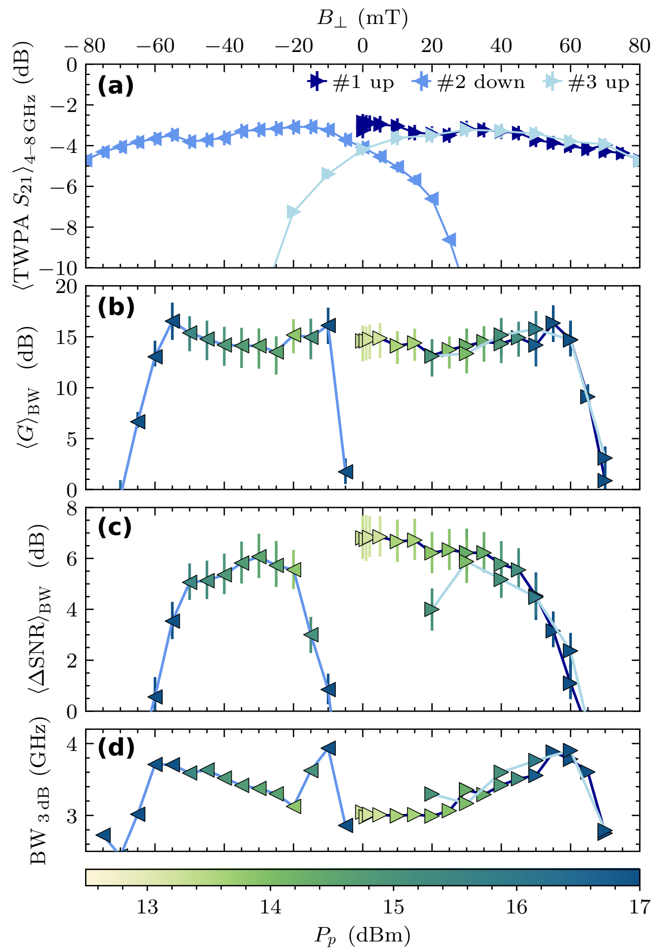

FIG. 4. (a) The $B_\perp$ dependence of $\langle \mathrm{TWPA}\, S_{21}\rangle_{4-8\,\mathrm{GHz}}$. The hysteresis is much more pronounced than for $B_{\parallel,1}$. (b) Corresponding gain curves at different $B_\perp$. The gain remains stable until a steep drop around 60 mT. Upon the downward sweep, the gain returns only after passing through zero field, around $B_\perp \approx -10$ mT, and behaves similarly for the subsequent upward sweep. (c) ΔSNR versus $B_\perp$ already decreases while gain remains stable, suggesting added noise consistent with vortices effectively raising the amplifier temperature. The initial ΔSNR is not recovered in subsequent sweeps. (d) $\mathrm{BW}_{3\,\mathrm{dB}}$ at different $B_\perp$, increasing until a sudden downturn at 60 mT. Hysteresis is not pronounced for $\mathrm{BW}_{3\,\mathrm{dB}}$.

and hysteresis [51], and there are field-dependent complex surface-impedance descriptions that include vortices (see Kwon *et al.* [50], whose approach could be integrated into ours in Appendix D), these models require many parameters (vortex viscosity, pinning potentials) and assumptions, e.g., about the current distribution in the ground plane. Observed catastrophic flux avalanches [52] could also complicate quantitative modeling, which we therefore do not pursue here.

Figure 4(b) shows the gain curves at different $B_\perp$. The gain remains stable up to around 60 mT, where a steep drop is observed. This drop could be due to vortices entering the NbTiN microstrip: the field H_s at which vortices are stable in the center of a strip of width W and coherence length ξ is given by (see Ref. [53] and the references therein)

$$H_s = \frac{2\Phi_0}{\pi W^2} \ln \frac{2W}{\pi \xi}, \tag{2}$$

which in our sample ($W = 340$ nm, $\xi = 4.9$ nm based on the critical-field value extrapolated at low temperature; see Appendix F) is of order 43 mT. If cooling occurs in a field below this value, as in our experiment, no vortices are expected to be present in the strip; an energy barrier impeding vortex entry is present even above this field, but it decreases with increasing field or in the presence of currents, e.g., the currents due to the pump. Therefore, at sufficiently high field $H \gtrsim H_s$, a configuration with vortices in the microstrip could be realized. Based on this estimate, improving the field compatibility could be achieved by reducing the microstrip width. However, this quickly becomes challenging from a fabrication perspective. Upon the downward sweep, the gain returns only around $B_\perp \approx -10$ mT, when the vortices created in the preceding upward sweep are expelled; the behavior is similar for the subsequent upward sweep. Figure 4(c) shows the SNR improvement as a function of $B_\perp$, which already decreases while the gain remains stable. This suggests that the vortices reduce the SNR by adding noise, rather than by reducing the gain or increasing the insertion loss. The ΔSNR starts to drop steeply already around 50 mT. The initial SNR improvement is not recovered in the subsequent sweeps. Figure 4(d) shows the bandwidth at different $B_\perp$, increasing until a sudden downturn at 60 mT. Hysteresis is not pronounced for the bandwidth, likely because the bandwidth is not directly field dependent, but rather depends on the optimized P_p.

In summary, for the $B_{\parallel,1}$ dependence, the $\langle G\rangle_{\mathrm{BW}}$ and $\langle \Delta\mathrm{SNR}\rangle_{\mathrm{BW}}$ plateaus align, while for $B_\perp$, ΔSNR decays before the gain does. This indicates that vortices may effectively add noise rather than simply adding attenuation. This is also apparent when comparing the $\langle \mathrm{TWPA}\, S_{21}\rangle_{4-8\,\mathrm{GHz}}$ values at which $\langle G\rangle_{\mathrm{BW}}$ plunges for in-plane versus out-of-plane fields.

VI. CONCLUSION AND OUTLOOK

We have shown that a kinetic inductance TWPA provides substantial SNR improvement in in-plane magnetic fields of up to 350 mT and in out-of-plane fields of up to 50 mT, an order-of-magnitude improvement over the bottleneck fields demonstrated for J-TWPAs (3 mT for the in-plane direction and 5 mT for the out-of-plane direction) [15]. With this operating range, it could be used in high-field experiments without magnetic shielding if positioned at some distance from the magnet center. The bandwidth can actually improve at intermediate in-plane fields with similar gain and added noise. We attribute this to increased

TWPA loss suppressing pump reflections and improving device performance.

While this KI-TWPA is not as field compatible as some demonstrated parametric amplifiers [16–20], it offers larger bandwidth and saturation power. The field compatibility is mostly limited by vortex losses due to the absence of vortex-trapping structures [54,55]. Our findings also suggest that reducing the microstrip width would likely improve the out-of-plane field compatibility; ultimately, this is limited by lithography, requiring the reliable realization of ~ 100 nm structures over the millimeter-scale length of the TWPA. Using an NbTiN or NbN ground plane with vortex traps could improve the in-plane field compatibility to several tesla. Out-of-plane fields will remain limiting: even thin-film NbTiN resonators with 100 nm width and distant ground planes show order-of-magnitude decreases in quality factor at 0.4 T [56].

The temperature dependence of the KI-TWPA shows effective operation up to 3 K, consistent with expectations given that the signal and idler input noise also scale with temperature in this experiment. The SNR improvement over the HEMTs is lost around 3 K for this reason. Whether mounting the TWPA at the cold plate (approximately 0.3 K) or still stage (approximately 1 K) could be beneficial depends on the second-stage noise temperature: with our measured $T_{\text{second}} \approx 13$ K, the ΔSNR at 1 K is still about 4 dB, but with an optimally biased state-of-the-art HEMT approaching 1.5 K noise temperature, the TWPA might not provide an improvement. However, the TWPA pump power does not necessarily have to be completely dissipated at the same temperature stage, but can instead be terminated elsewhere, as in this work. Similarly, the idler and signal band do not have to be thermalized at the same stage as the TWPA, which could restore the noise advantage even if the TWPA is mounted at higher temperature. Superconducting cables make this possible because they combine low loss with low thermal conductivity. Mounting at different stages can be useful for a variety of reasons, e.g., distance from a magnet or space constraints at the mixing chamber.

Although this work presents data from a single device, we find that key limits in the temperature and magnetic field dependence can be understood based on design and material parameters. Therefore, our work can guide the design of future devices with higher magnetic field and temperature limits. The demonstrated magnetic field and temperature performance already showcase the potential of KI-TWPAs to replace or complement existing amplifiers in demanding experimental setups.

ACKNOWLEDGMENTS

We thank Timur Zent for help with the assembly of the cryogenic setup. This project has received funding from the European Research Council (ERC) under the European Union’s Horizon 2020 research and innovation program (Grant Agreement No. 741121) and was also funded by the Deutsche Forschungsgemeinschaft (DFG, German Research Foundation) under CRC 1238—277146847 (Subproject B01), as well as under Germany’s Excellence Strategy–Cluster of Excellence Matter and Light for Quantum Computing (ML4Q) EXC 2004/1 - 390534769. Devices were fabricated at the Jet Propulsion Laboratory, California Institute of Technology, under a contract with the National Aeronautics and Space Administration (80NM0018D0004).

The project was conceived by C.D. and Y.A. in coordination with F.F. and P.D.. The TWPAs were designed and fabricated by P.D., F.F., and H.G.L. at JPL. The measurements were performed by L.M.J. and C.D. in Cologne with support from F.F. and P.D.. The dc magnetic measurements of the superconducting films were performed by S.P at Caltech. The data were analyzed by L.M.J. and C.D. with support from F.F. and P.D.. G.C. provided theoretical support for the project. The manuscript was written by L.M.J., F.F., and C.D. with input from all coauthors.

DATA AVAILABILITY

Datasets, analysis code, and code for the TWPA model are made available as PYTHON files and Jupyter notebooks that reproduce the figures of this manuscript [57]. The setup was controlled using QCoDeS [58] drivers, and the measurements were run using Quantify-core [59].

APPENDIX A: DEVICE DESCRIPTION AND MEASUREMENT SETUP

The device is a kinetic inductance traveling-wave parametric amplifier fabricated at the NASA Jet Propulsion Laboratory, similar to the device described in Ref. [3], based on design ideas outlined in Ref. [60]. It consists of a microstrip transmission line with an NbTiN center conductor (35 nm thick, 340 nm wide) and an Nb ground plane (350 nm thick), separated by a 100 nm-thick amorphous-silicon dielectric layer. The kinetic inductance at low field and temperature predominantly stems from the center conductor. The center conductor has periodic capacitive-loading structures to engineer a bandgap around 12 GHz, which enables phase matching for four-wave mixing when pumped near the band edge. Neither the center conductor (which has wider areas at the launchers) nor the ground plane incorporates vortex-trapping structures, as the device was not specifically designed with magnetic field compatibility in mind. This also explains the choice of niobium as the ground-plane material. Because of the high charge-carrier density of thick niobium films, their kinetic inductance can be neglected, simplifying the design and modeling of the device. While an NbTiN ground plane would improve the field compatibility and allow higher-temperature operation, the design would require more complex modeling of the kinetic inductance contribution of both layers, in particular because the current density in the ground plane would not be uniform. Our work therefore provides a baseline for future KI-TWPA designs optimized for field compatibility.

The device is mounted in a copper box that is thermally anchored to the mixing chamber of an Oxford Instruments Triton 400 dilution refrigerator inside a fast-loading puck. A 6 T-1 T-1 T vector magnet provides magnetic fields, with the 6 T axis corresponding to $B_{\parallel,1}$ (see Fig. 1). The alignment of the device to the magnetic field axes is imperfect; based on previous experiments, the misalignment is estimated to be below 2° [33,34], but it could be greater here because the TWPA might not be perfectly aligned to the box, as it is glued in place. Some observed hysteresis is likely intrinsic to the vector magnet, but most of the observed effects originate from the device itself.

The measurement setup is shown in Fig. 5. Two diplexers (DPX1) sandwich the TWPA to couple the pump in and out, preventing saturation of subsequent amplifiers. These commercial diplexers are not specified for cryogenic operation, but they do not show strong changes in transmission during cooldowns. An additional diplexer (DPX2) thermalizes the idler band at the TWPA input to the mixing chamber. The frequency ranges of the diplexers limit f_p to approximately 9–11 GHz.

The pump power P_p is specified throughout this work as the power at the microwave source (approximately 15 dBm). The line has one attenuator of 20 dB at the 4 K stage, but including approximately 20 dB of losses in stainless-steel coaxial cable and additional components, P_p at the TWPA input is approximately −25 dBm. We did not prioritize calibrating lines for accurate device-power estimation. We also did not prioritize estimating the saturation power in this study, as for our planned typical use case, the TWPA saturation power is sufficiently large that it would not be a limiting factor. We took some VNA power scans to look for saturation effects and did not observe saturation up to the maximum VNA output power of 10 dBm (approximately −60 dBm at the TWPA input), consistent with expectations. Measurements of the TWPA gain were generally performed with a probe power of −40 dBm at the VNA, corresponding to approximately −110 dBm at the TWPA input, which gave sufficient signal-to-noise ratio for the measurements and is far below the expected saturation power. Faramarzi *et al.* [3] found that the output saturation power is approximately 20 dB below the pump power. Since at higher fields and temperatures we find that the required pump power increases, one could speculate that saturation power increases as well, but we do not have measurements to confirm this.

The thermalization of the termination of the pump tone after the TWPA requires careful consideration for KI-TWPAs. The significant pump power cannot be thermalized at the mixing chamber, as it would exceed the cooling capacity even in large cryostats. We attached thermalization to the cold plate, though in retrospect, still-stage thermalization would be preferable to reduce the cold-plate heat load. As the mixing-chamber temperature also increases with pump power, we capped P_p at 17 dBm to maintain base temperatures below 50 mK.

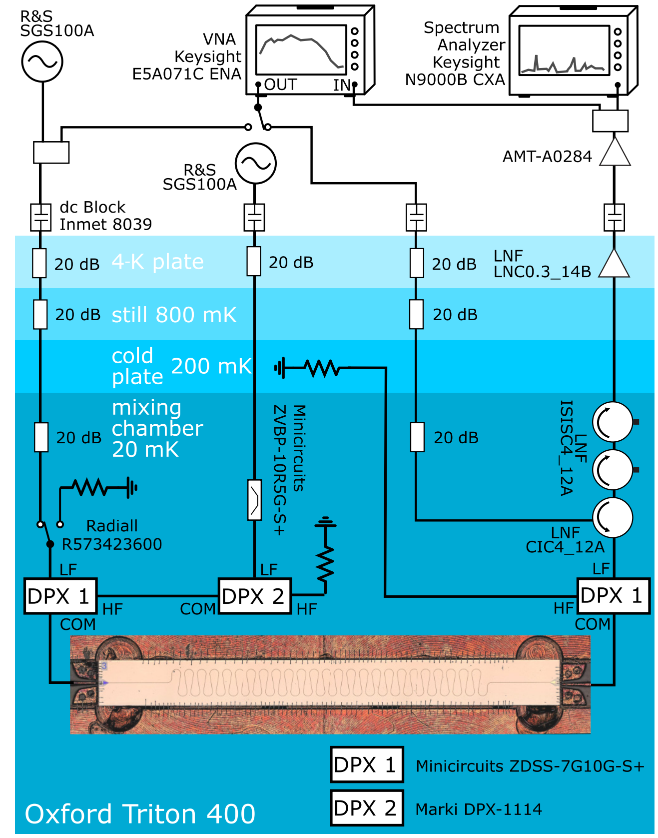

FIG. 5. Schematic of the cryogenic measurement setup, including input and output lines, attenuators, circulators, and the amplification chain. The circulator at the TWPA output enables transmission and reflection measurements without internal switching. Signal, pump, and idler routing through diplexers is necessary because of the high pump power and in order to thermalize the idler input to the mixing chamber. Diplexers marked DPX1: low band up to 7.5 GHz, high band 10.5-20 GHz. DPX2: low band up to 11 GHz, high band 14-30 GHz.

For calibration, we measured a “background transmission” through our setup with a short cable replacing the TWPA in the loading puck. This background was subtracted to calculate the net TWPA gain and the added noise. To exclude the possibility that temperature or field affects other components of the setup, we performed temperature and field scans in this bypass configuration (see Appendix H). We found negligible temperature and magnetic field dependence of the transmission in the 4–8-GHz band. We attribute the small changes in transmission to the circulators.

APPENDIX B: TWPA PUMP SETTINGS AND OPTIMIZATION

To optimize TWPA performance, we measured $\langle \Delta \mathrm{SNR} \rangle_{4-8\,\mathrm{GHz}}$ for various P_p and f_p settings at base temperature and zero field. The results are summarized in Fig. 6. The choice of $\langle \Delta \mathrm{SNR} \rangle_{4-8\,\mathrm{GHz}}$ as the figure of merit is practical: the lower limit (4 GHz) is imposed by the circulator specifications, while this setup achieves poor SNR improvement above 8 GHz. This figure of merit is a good compromise because it rewards both a larger bandwidth and a better overall SNR improvement. The data show that the SNR improvement exhibits a chaotic landscape rather than a simple dependence on P_p and f_p, which complicates the optimization of these settings. While this requires finding optimum settings that can also vary with field and temperature, once optimum settings are found, performance is stable over time. We also thermally cycled the device multiple times during the weeks in which the data presented here were taken and found that device performance was reproducible, although optimum pump settings varied slightly after thermal cycling.

We used the Nelder-Mead algorithm [61] to find optimal P_p and f_p for every magnetic field and temperature, using $\langle \Delta \mathrm{SNR} \rangle_{4-8\,\mathrm{GHz}}$ as the figure of merit. P_p was limited to a maximum of 17 dBm to prevent excessive heating of the fridge. The setup could have less attenuation on the pump input line, and one could thermalize the pump at the still plate to achieve better performance at points were we reached this maximum power. We used multiple starting points during the field and temperature scans to avoid becoming trapped in local maxima. For the data in Fig. 3, for example, we optimized around three different f_p values (10.3 GHz, 10.75 GHz, and 11.15 GHz). Around all three frequencies, we could find pump powers for which the TWPA gain was above 10 dB. The optimum frequencies did not shift strongly with magnetic field. The results of different optimizations from these slightly varied initial conditions were consistent, showing that we indeed find robust maxima.

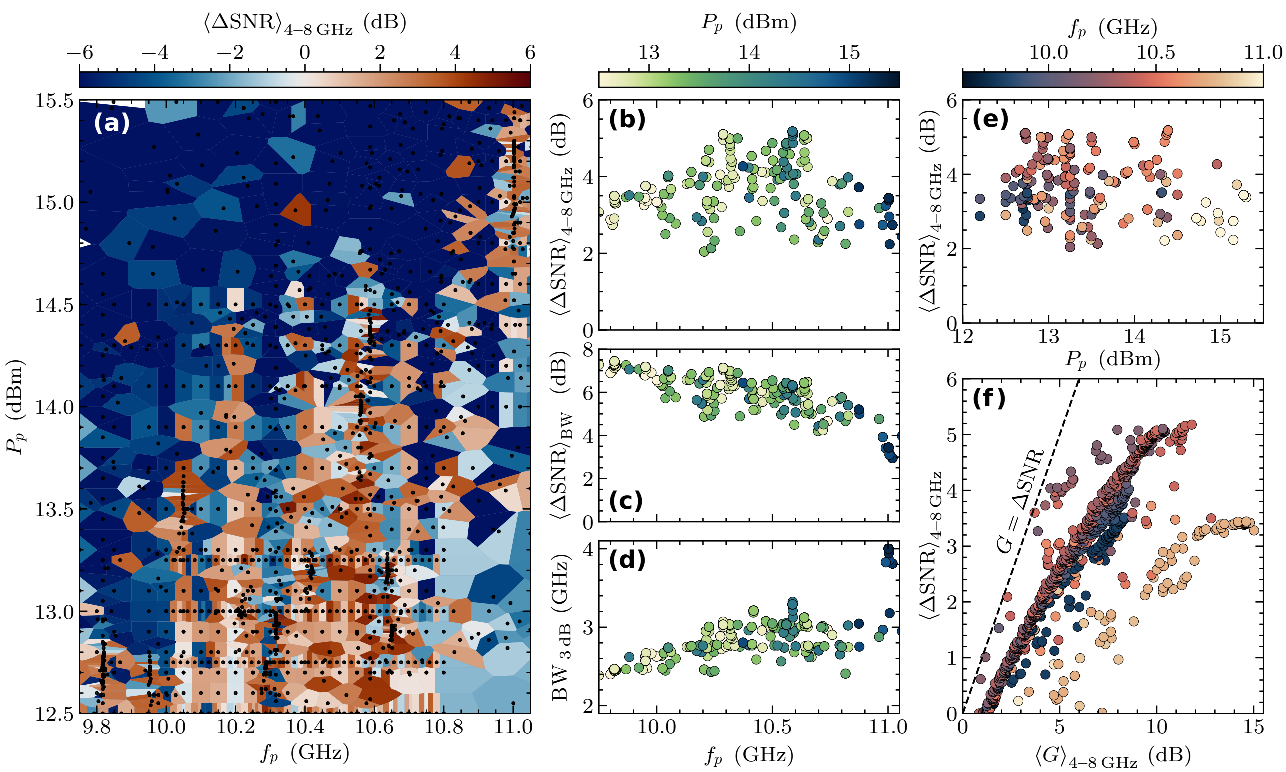

FIG. 6. (a) Mean SNR improvement in the 4–8-GHz band, $\langle \Delta \mathrm{SNR} \rangle_{4-8\,\mathrm{GHz}}$, versus pump power P_p and frequency f_p at zero field. Measurements are indicated with black points. The color map indicates the SNR improvement of the nearest measured point, revealing a chaotic landscape. Panels (b)–(d) show $\langle \Delta \mathrm{SNR} \rangle_{4-8\,\mathrm{GHz}}$, the mean within the bandwidth $\langle \Delta \mathrm{SNR} \rangle_{\mathrm{BW}}$, and the bandwidth $\mathrm{BW}_{3\,\mathrm{dB}}$ for the same data points as a function of f_p, with P_p color coded. With increasing f_p, $\mathrm{BW}_{3\,\mathrm{dB}}$ can be improved, but $\langle \Delta \mathrm{SNR} \rangle_{\mathrm{BW}}$ is reduced. This leads to optimum frequencies for $\langle \Delta \mathrm{SNR} \rangle_{4-8\,\mathrm{GHz}}$. (e) $\langle \Delta \mathrm{SNR} \rangle_{4-8\,\mathrm{GHz}}$ as a function of P_p, with f_p color coded, showing that there is no clear optimum power range. (f) SNR improvement versus gain, showing clearly that, for the bulk of the data, there is a clear relationship between the two, consistent with a relatively fixed TWPA noise power. The higher-f_p data show a different trend, suggesting that the added noise for higher f_p and P_p is larger.

Occasionally $\langle \Delta \mathrm{SNR} \rangle_{4-8\,\mathrm{GHz}}$ exceeded $\langle G \rangle_{4-8\,\mathrm{GHz}}$, occurring when the device switched state between the gain and noise measurements under strong drive. Thus, there are occasional outliers in the $\langle \Delta \mathrm{SNR} \rangle_{4-8\,\mathrm{GHz}}$ datasets, but we generally repeated measurements, and the switches are rare and not systematic. Figure 6(f) shows the general relationship between mean gain and $\langle \Delta \mathrm{SNR} \rangle_{4-8\,\mathrm{GHz}}$ characteristic of the TWPA, with some outliers. High-pump-frequency data follow a curve with lower $\langle \Delta \mathrm{SNR} \rangle_{4-8\,\mathrm{GHz}}$ saturation, possibly due to heating effects at higher required pump powers.

APPENDIX C: TWPA INSERTION LOSS VERSUS TEMPERATURE

This appendix presents detailed TWPA insertion-loss data as a function of frequency and temperature. The insertion loss is similar to that in the setup of Ref. [3]. Figure 7(a) shows gradual transmission breakdown, consistent with the niobium ground plane T_c of approximately 9.1 K.

Figure 7(b) shows mean insertion loss $\langle \mathrm{TWPA}\, S_{21} \rangle_{4-8\,\mathrm{GHz}}$ versus temperature and compares it to our model (detailed in Appendix D). The model parameters are primarily based on nominal dimensions and material properties rather than a fit to the data. Only dielectric loss and a kinetic inductance scaling factor for the NbTiN α_{KI} were adjusted to match the data. The dielectric loss was assumed to arise primarily from the thin dielectric in the inverse microstrip, and this was adjusted to match TWPA $S_{21}(f)$ at low temperature. α_{KI} was adjusted to match the bandgap frequency measured in dipstick measurements [Fig. 7(e)]. Dipstick data were acquired before TWPA mounting in the dilution refrigerator. The need for the α_{KI} factor could also be due to slight variations in the NbTiN film thickness or normal-state conductivity across a wafer. The smoother TWPA $S_{21}(f)$ in the dipstick data suggests that

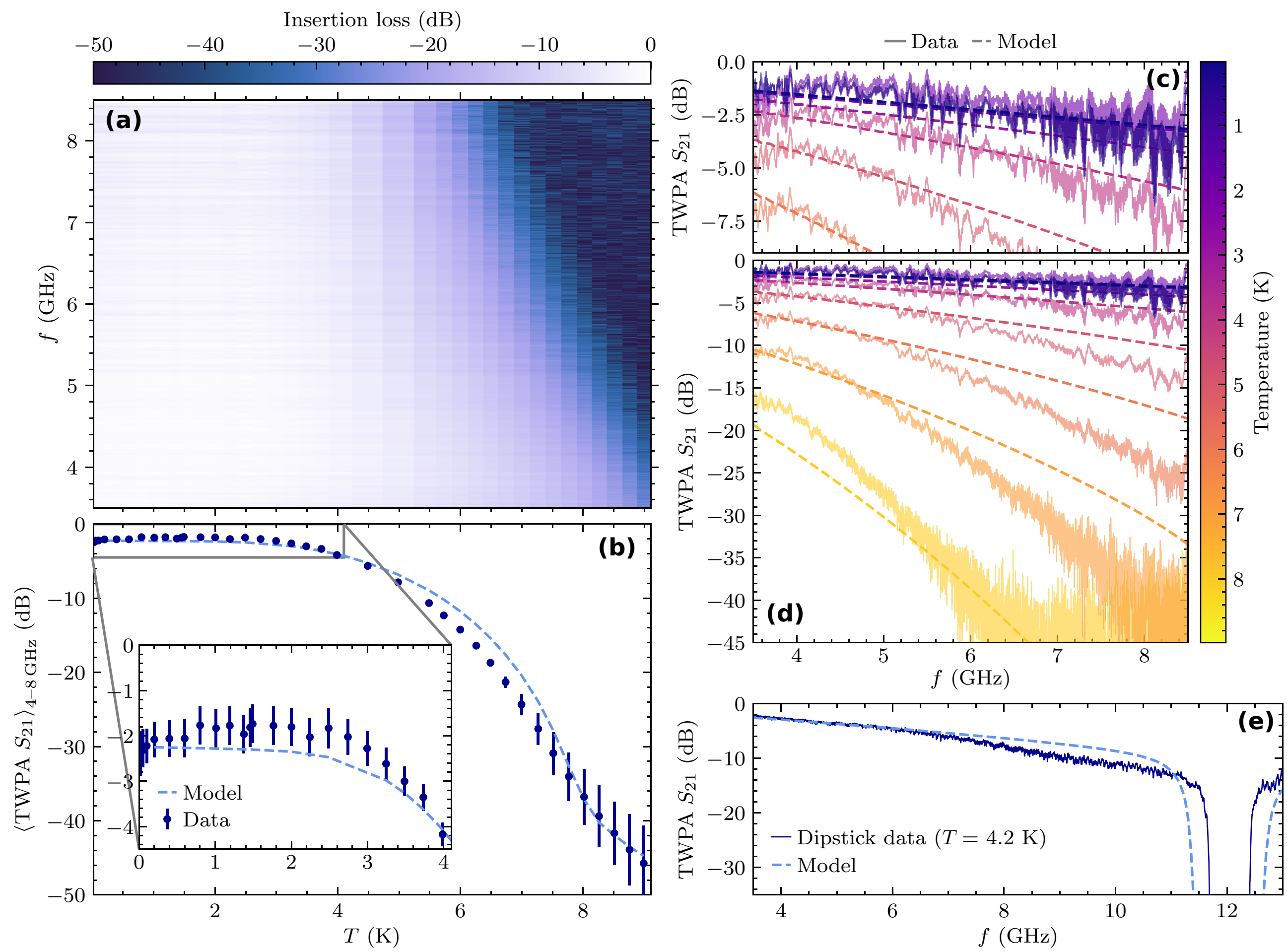

FIG. 7. (a) TWPA S_{21} as a function of temperature T and f. (b) $\langle \mathrm{TWPA}\, S_{21} \rangle_{4-8\,\mathrm{GHz}}$ for different T. Initially, there is a slight decrease in insertion loss that could be due to TLS saturation. At higher T, transmission breaks down because of quasiparticle losses. (c),(d) TWPA S_{21} as a function of f for different T, showing both the data and the model. The data in the top panel are the same as those in the bottom panel but plotted on a different vertical scale. (e) TWPA S_{21} as a function of f for a dipstick measurement in liquid helium, showing the bandgap frequency. The model including the bandgap is shown, as we chose α_{KI} to match the data.

the impedance mismatches outside the TWPA in the dilution refrigerator (e.g., diplexers and circulators) are non-negligible. The diplexers prevent the observation of the bandgap in transmission measurements in the dilution refrigerator. Measuring the bandgap in transmission without diplexers could improve our understanding of the temperature (and magnetic field) dependence.

The model matches the $\langle \mathrm{TWPA}\, S_{21} \rangle_{4-8\,\mathrm{GHz}}$ data reasonably well, but we observe notable deviations when considering the full frequency dependence at different temperatures [Figs. 7(c) and 7(d)] rather than average insertion loss. At low temperatures (below 2 K), an initial insertion-loss decrease likely reflects two-level fluctuator saturation, which is not included in the model [62,63]. At higher temperatures, the data show stronger high-frequency losses.

APPENDIX D: MODELING TWPA S_{21}

We model the TWPA transmission S_{21} to understand the temperature and magnetic field dependence, following Ref. [64]. The model uses Mattis-Bardeen theory [48] to calculate superconductor surface impedance and the temperature and field dependence of the superconducting gap. Whereas the temperature dependence is reasonably described, the magnetic field dependence is more complex and cannot be explained by gap suppression alone. Field-induced gap suppression without an increase in temperature does not substantially increase the surface resistance. Overall, the surface resistance changes significantly only near B_c. The limitations of the model in describing magnetic field dependence stem from neglecting vortex effects and screening currents in the ground plane, which increase pair breaking. More sophisticated models such as that of Ref. [50] could describe the data by combining two-fluid models with a Coffey-Clem model [65] for vortex dynamics and losses. However, too many free parameters would be required; we therefore do not pursue this approach, as it goes beyond the scope of the present work.

Rather than fitting the model to the data, we choose physically reasonable values based on nominal device dimensions and material properties. We varied only two parameters, the dielectric loss in the thin dielectric layer and a kinetic inductance scaling factor α_{KI} for the NbTiN, to match the low-temperature insertion loss and the bandgap frequency measured in a dipstick setup. Model parameters and values are listed in Table I. Model code is provided in the data and software repository accompanying this work [57]. While a full parameter optimization could improve the fit to the data, crucial bandgap-frequency data that could constrain the parameters could not be measured because of diplexers in our setup.

The calculation of TWPA S_{21} for each frequency follows these steps.

TABLE I. Summary of the model parameters with chosen values.

Parameter	Value	Description
TWPA design parameters		
w	340 nm	Microstrip width
t_s	35 nm	Strip thickness (NbTiN)
t_g	350 nm	Ground-plane thickness (Nb)
h	100 nm	Dielectric thickness
d	2.21 μm	Unit-cell period
n_{stubs}	59	Number of stubs per cell
n_{cells}	80	Total number of unit cells
l_0	10.8 μm	Average stub length
l_a	2.08 μm	Modulation amplitude
Material property parameters		
T_c^{NbTiN}	12.0 K	Critical temperature (NbTiN)
T_c^{Nb}	9.15 K	Critical temperature (Nb)
$2\Delta_0/k_B T_c$	3.5	Gap ratio (both materials)
$\sigma_n^{\mathrm{NbTiN}}$	$0.56\times10^6\ \mathrm{S\,m^{-1}}$	Normal-state conductivity (NbTiN)
σ_n^{Nb}	$5\times10^6\ \mathrm{S\,m^{-1}}$	Normal-state conductivity (Nb)
α_{KI}	1.6	Kinetic inductance enhancement factor
$\varepsilon_{r,\mathrm{sub}}$	10.3	Substrate relative permittivity
$\varepsilon_{r,\mathrm{super}}$	11.4	Superstrate relative permittivity
$\tan\delta_{\mathrm{sub}}$	1×10^{-5}	Substrate loss tangent
$\tan\delta_{\mathrm{super}}$	0.03	Superstrate loss tangent

(1) Calculate the superconducting gap $\Delta(T,B)$ for both Nb and NbTiN materials (Appendix D 1).

(2) Compute surface impedances $Z_s = R_s + jX_s$ using Mattis-Bardeen theory with the temperature- and field-dependent gaps (Appendix D 2).

(3) Calculate transmission-line parameters (characteristic impedance Z_0, propagation constant γ), including kinetic inductance contributions (Appendix D 3).

(4) Use cascaded ABCD matrices to model the complete device with modulated unit cells (Appendix D 4).

(5) Convert the total ABCD matrix to the S_{21} parameter.

1. Temperature and field dependence of the gap

This section explains how we model superconducting gap parameter $\Delta(T,B)$ as a function of temperature and magnetic field, which is the key input parameter for the Mattis-Bardeen surface-impedance calculations. We have estimates for the T_c of NbTiN and Nb based on our dc characterization and cooldown data (see Appendices F and G). For NbTiN, we use $T_c = 12.0$ K based on the cooldown data (consistent with Appendix G), while our dc characterization yielded a slightly higher value, possibly due to variations in film properties across the wafer or different measurement techniques. For both materials, we assume the BCS gap-to-critical-temperature ratio $2\Delta_0/k_BT_c = 3.5$ as an approximation; the actual values of $2\Delta_0/k_BT_c$ are typically larger and can vary depending on film thickness and quality [66,67].

For the temperature dependence of the gap, we assume that [68]

$$\Delta(T) = \Delta_0 \tanh\left(1.74\sqrt{\frac{T_c}{T} - 1}\right),$$

where T_c is the critical temperature and Δ_0 is the gap at zero temperature. For magnetic field suppression, the functional form depends on field orientation: for fields not too close to the respective critical fields, out-of-plane fields reduce the gap linearly as

$$\Delta(B_\perp) = \Delta_0\left(1 - \frac{B_\perp}{B_{c\perp}}\right),$$

while in-plane fields cause a Ginzburg-Landau-type gap suppression,

$$\Delta(B_\parallel) = \Delta_0\sqrt{1 - \left(\frac{B_\parallel}{B_{c\parallel}}\right)^2}.$$

where $B_{c\perp}$ and $B_{c\parallel}$ are effective critical magnetic fields in the two directions (the effective critical fields are proportional to, but larger than, the actual ones—see Ref. [15]). We note that, for the magnetic field dependence, this form of gap suppression is ultimately not sufficient to explain the observed transmission loss, as discussed in Appendix E.

2. Mattis-Bardeen surface impedance

We use Mattis-Bardeen theory to calculate the surface impedance $Z_s = R_s + jX_s$ for both the NbTiN strip and the Nb ground plane, which provides the electromagnetic losses and kinetic inductance contributions needed for the transmission-line parameter calculations. The key material parameters are the normal-state conductivities σ_n and the superconducting gaps $\Delta(T, B)$, as well as the angular frequency ω and the temperature T. For superconducting materials with gap parameter $\Delta(T, B)$, the surface impedance is calculated as

$$Z_s = R_s + jX_s = \sqrt{\frac{j\omega\mu_0}{\sigma_1 - j\sigma_2}},$$

where σ_1 and σ_2 are the real and imaginary parts of the complex conductivity.

The numerical implementation uses dimensionless variables $\tilde{E} = E/\Delta$, $\tilde{\omega} = \hbar\omega/\Delta$, and $\tilde{T} = k_BT/\Delta$, where E is the quasiparticle energy, ω is the angular frequency, and T is the temperature. The complete Mattis-Bardeen expressions [48,69] are

$$\frac{\sigma_1}{\sigma_n} = \frac{2}{\tilde{\omega}}\int_1^\infty \frac{[f(\tilde{E}) - f(\tilde{E}+\tilde{\omega})](\tilde{E}(\tilde{E}+\tilde{\omega})+1)}{\sqrt{\tilde{E}^2-1}\sqrt{(\tilde{E}+\tilde{\omega})^2-1}}\,d\tilde{E}$$
$$+ \frac{\theta(\tilde{\omega}-2)}{\tilde{\omega}}\int_{1-\tilde{\omega}}^{-1} \frac{[1 - 2f(\tilde{E}+\tilde{\omega})](\tilde{E}(\tilde{E}+\tilde{\omega})+1)}{\sqrt{\tilde{E}^2-1}\sqrt{(\tilde{E}+\tilde{\omega})^2-1}}\,d\tilde{E},$$
$$\frac{\sigma_2}{\sigma_n} = \frac{1}{\tilde{\omega}}\int_{-1}^{1-\tilde{\omega}} \frac{[1 - 2f(\tilde{E}+\tilde{\omega})](\tilde{E}(\tilde{E}+\tilde{\omega})+1)}{\sqrt{1-\tilde{E}^2}\sqrt{(\tilde{E}+\tilde{\omega})^2-1}}\,d\tilde{E},$$

where $f(\tilde{E}) = 1/(e^{\tilde{E}/\tilde{T}} + 1)$ is the Fermi-Dirac distribution function, σ_n is the normal-state conductivity, and $\theta(\tilde{\omega} - 2)$ is the Heaviside step function. The second term in σ_1 represents pair-breaking processes that become active when $\tilde{\omega} > 2$ (i.e., $\hbar\omega > 2\Delta$). Our implementation neglects this pair-breaking term because it is not significant in our frequency range of interest (4–8 GHz), where $\tilde{\omega} \ll 1$ for both materials except near T_c or B_c; thus, near the transition, the model underestimates pair breaking.

The integrals are evaluated numerically using adaptive quadrature with physics-motivated integration points based on the gradient of the integrand and regularization (adding small complex numbers to the integrand) to better handle singularities. For the thin NbTiN and Nb films used in our device, finite-thickness corrections are applied to account for the reduced dimensionality compared to bulk superconductors; see the next subsection. The resulting surface impedances $Z_{s,s}$ (strip) and $Z_{s,g}$ (ground plane) are input variables for the calculation of the transmission-line parameters in the following section.

For magnetic field effects beyond gap suppression, additional terms could be incorporated to account for vortex-induced losses and increased pair breaking, but we found that the experimental data available would not allow for a satisfactory understanding of these microscopic effects.

3. Transmission-line parameters of the inverse microstrip

We calculate the distributed transmission-line parameters of the inverse microstrip, characteristic impedance Z_0 and propagation constant $\gamma = \alpha + j\beta$, which are required for the ABCD-matrix modeling of the TWPA unit cells. The inverse-microstrip geometry features a superconducting strip positioned between the ground plane and the substrate, in contrast to a conventional microstrip where the strip is on top. The key geometric parameters of our device are the strip width w, dielectric thickness h, strip thickness t_s, and ground-plane thickness t_g. We start with the baseline transmission-line parameters calculated using the Hammerstad-Jensen model [70], then apply superconducting corrections to account for the kinetic inductance contributions from both the strip and the ground plane.

The Hammerstad-Jensen model first calculates thickness-corrected widths to account for finite conductor thickness:

$$\Delta u_1 = \frac{t_s/h}{\pi} \ln\left(1 + \frac{4e}{(t_s/h)\coth^2(\sqrt{6.517u})}\right),$$
$$\Delta u_r = \frac{1}{2}\left(1 + \frac{1}{\cosh\sqrt{\varepsilon_r - 1}}\right)\Delta u_1,$$

where $u = w/h$ is the normalized strip width, t_s is the strip thickness, h is the dielectric thickness, and ε_r is the relative permittivity.

The effective dielectric constant for the baseline geometry is

$$\varepsilon_{\text{eff},0} = \frac{\varepsilon_r + 1}{2} + \frac{\varepsilon_r - 1}{2}\left(1 + \frac{10}{u_r}\right)^{-ab},$$
$$a = 1 + \frac{1}{49}\ln\left[\frac{u_r^4 + (u_r/52)^2}{u_r^4 + 0.432}\right] + \frac{1}{18.7}\ln\left[1 + \left(\frac{u_r}{18.1}\right)^3\right],$$
$$b = 0.564\left(\frac{\varepsilon_r - 0.9}{\varepsilon_r + 3}\right)^{0.053},$$

where $u_r = u + \Delta u_r$ is the thickness-corrected normalized width. We use separate dielectric properties for the substrate and superstrate: relative permittivities $\varepsilon_{r,\text{sub}}$ and $\varepsilon_{r,\text{super}}$ and loss tangents $\tan\delta_{\text{sub}}$ and $\tan\delta_{\text{super}}$.

The effective dielectric constant for mixed dielectrics is calculated by weighting the substrate and superstrate contributions:

$$\varepsilon_{\text{eff}} = \varepsilon_{r,\text{sub}} q_{\text{sub}} + \varepsilon_{r,\text{super}} q_{\text{super}},$$

where the field-filling factors q_{sub} and q_{super} are defined below.

The characteristic impedance of the baseline microstrip is

$$Z_{0,\text{base}} = \frac{\eta_0}{2\pi\sqrt{\varepsilon_{\text{eff},0}}}\ln\left(\frac{F_u}{u_r} + \sqrt{1 + \left(\frac{2}{u_r}\right)^2}\right),$$

where $\eta_0 = 377\ \Omega$ is the free-space impedance and

$$F_u = 6 + (2\pi - 6)\exp(-(30.666/u_r)^{0.7528}).$$

From the baseline parameters, we extract the geometric inductance and capacitance:

$$L'_{\text{geom}} = \frac{Z_{0,\text{base}}}{v_{\text{ph,base}}} = \frac{Z_{0,\text{base}}\sqrt{\varepsilon_{\text{eff},0}}}{c},$$
$$C' = \frac{1}{Z_{0,\text{base}} v_{\text{ph,base}}} = \frac{\sqrt{\varepsilon_{\text{eff},0}}}{Z_{0,\text{base}} c}.$$

The kinetic inductance contributions are calculated from the surface impedances $Z_{s,s}$ and $Z_{s,g}$ and are added to the geometric inductance. The surface inductance is corrected for finite-thickness films using the Pearl effect:

$$\mathcal{L}_{\text{surf}} = \mu_0 \lambda \coth\left(\frac{t}{\lambda}\right),$$

where μ_0 is the permeability of free space, λ is the penetration depth, and t is the film thickness. The penetration depth λ is calculated from the imaginary part of the surface impedance:

$$\lambda = \frac{\text{Im}(Z_{\text{s,s}})}{\omega\mu_0}, \qquad \lambda_{\text{g}} = \frac{\text{Im}(Z_{\text{s,g}})}{\omega\mu_0},$$

where ω is the angular frequency, $Z_{s,s}$ is the surface impedance of the strip, and $Z_{s,g}$ is the surface impedance of the ground plane.

The total distributed inductance combines geometric and kinetic components:

$$L' = L'_{\text{geom}} + \frac{\mathcal{L}_{\text{surf},s}\alpha_{\text{KI}}}{w} + \frac{\mathcal{L}_{\text{surf,g}}}{w},$$

where α_{KI} is a kinetic inductance enhancement factor for the thin NbTiN center conductor. It was one of two parameters varied to match the model to the data. Without this additional factor, the TWPA bandgap in the model would not match the helium dipstick measurement presented in Fig. 7(e). It is not unplausible that the model underestimates the kinetic inductance. This could be due to variations in thickness or conductivity, as there are variations in film properties across a wafer. Additionally, a nonuniform current distribution in the center-conductor strip could also increase the effective kinetic inductance. We decided to include this factor rather than attempt to adjust the nominal parameters. We also assume that the current distribution in the ground plane is uniform across the width of the center conductor. This is an approximation, and the current will probably spread out, especially once λ_{g} approaches the ground-plane thickness t_g. This could partly offset increases in the kinetic inductance of the ground plane that are expected with increasing temperature and magnetic field.

We include both dielectric and conductor loss in the real part α of the complex propagation constant $\gamma = \alpha + j\beta$.

The two loss contributions can be added: $\alpha = \alpha_d + \alpha_c$. Dielectric losses arise from the finite loss tangents of the substrate and superstrate materials, weighted by their respective field-filling factors:

$$q_{\text{sub}} = \frac{1}{2} + \frac{1}{4}\left(1 - \tanh\left(\frac{1}{2}\ln\left(\frac{\varepsilon_{\text{sub}}}{\varepsilon_{\text{super}}}\right)\right)\right)\frac{1+\ln(u^2)}{1+10/u},$$

$$q_{\text{super}} = 1 - q_{\text{sub}},$$

$$\alpha_d = \frac{\pi f}{c}\sqrt{\varepsilon_{\text{eff}}}(q_{\text{sub}}\tan\delta_{\text{sub}} + q_{\text{super}}\tan\delta_{\text{super}}),$$

where q_{sub} and q_{super} are the field-filling factors in the substrate and the superstrate, respectively. Conductor losses are calculated from the real parts of the surface impedances:

$$\alpha_c = \frac{R_s^{(s)}/w + R_s^{(g)}/w}{Z_0}\sqrt{\varepsilon_{\text{eff}}},$$

where $R_s^{(s)} = \text{Re}(Z_{s,s})$ and $R_s^{(g)} = \text{Re}(Z_{s,g})$ are the surface resistances of the strip and the ground plane, respectively. These losses are incorporated into the complex characteristic impedance by calculating the resistance and conductance per unit length: $R' = \alpha_c Z_0$ and $G' = 2\alpha_d/Z_0$. The complex characteristic impedance is then calculated:

$$Z_0^{\text{complex}} = \sqrt{\frac{R' + j\omega L'}{G' + j\omega C'}}.$$

These transmission-line parameters (Z_0, γ) serve as inputs for the ABCD-matrix formalism described in the next section.

4. ABCD-matrix formalism to calculate S_{21}

Using the transmission-line parameters from the previous section (characteristic impedance Z_0 and propagation constant $\gamma = \alpha + j\beta$), we model the TWPA using cascaded ABCD matrices to calculate the overall S_{21}. The TWPA modulation is implemented using a unit cell with periodically spaced capacitive stubs.

For a transmission-line segment of length d, the ABCD matrix is

$$\begin{bmatrix} A & B \\ C & D \end{bmatrix}_{\text{line}} = \begin{bmatrix} \cosh(\gamma d) & Z_0\sinh(\gamma d) \\ (1/Z_0)\sinh(\gamma d) & \cosh(\gamma d) \end{bmatrix}.$$

For a capacitive stub of length l_s with stub admittance $Y_{\text{stub}} = j(2/Z_0)\tan(\beta l_s)$, the ABCD matrix is

$$\begin{bmatrix} A & B \\ C & D \end{bmatrix}_{\text{stub}} = \begin{bmatrix} 1 & 0 \\ Y_{\text{stub}} & 1 \end{bmatrix}.$$

The unit-cell structure consists of transmission-line segments with stub spacing d and contains n_{stubs} stubs. The total device contains n_{cells} unit cells. The modulation of stub lengths follows a sinusoidal pattern:

$$l_i = l_0 + l_a \sin\left(2\pi\frac{i}{n_{\text{stubs}}}\right),$$

where l_i is the stub length of the ith stub, l_0 is the average stub length, and l_a is the modulation amplitude.

The unit-cell matrix is constructed by cascading (matrix multiplication) the transmission line segments and stub matrices:

$$\mathbf{A}_{\text{cell}} = \mathbf{A}_{\text{line},1/2}\prod_{i=1}^{n_{\text{stubs}}}(\mathbf{A}_{\text{stub},i}\mathbf{A}_{\text{line}}),$$

where $\mathbf{A}_{\text{line},1/2}$ represents the initial half-length transmission-line segment. For the complete TWPA with n_{cells} unit cells, the total ABCD matrix is computed using matrix exponentiation:

$$\mathbf{A}_{\text{total}} = \mathbf{A}_{\text{cell}}^{n_{\text{cells}}}.$$

Finally, the S_{21} parameter is calculated from the total ABCD matrix assuming a 50 Ω environment:

$$S_{21} = \frac{2}{A + B/Z_0^{\text{env}} + CZ_0^{\text{env}} + D},$$

where $Z_0^{\text{env}} = 50\,\Omega$.

APPENDIX E: TWPA INSERTION LOSS VERSUS MAGNETIC FIELD

This appendix discusses TWPA insertion loss as a function of field for the three orthogonal magnetic field directions. Although we did not find a model that describes the data with satisfying accuracy (unlike for the temperature dependence), the main features can be understood qualitatively and generally follow expectations.

1. $B_{\parallel,1}$ direction

Figure 8 shows TWPA S_{21} for a $B_{\parallel,1}$ range beyond where the TWPA provides gain (as presented in the main text), up to transmission breakdown. Figure 8(b) shows mean insertion loss $\langle\text{TWPA}\,S_{21}\rangle_{4-8\,\text{GHz}}$ for different sweeps, revealing hysteresis that likely indicates that vortices play a role, even at relatively low $B_{\parallel,1}$. This at least partially arises from misalignment of the sample plane to $B_{\parallel,1}$; this becomes clearer when comparing it to the $B_{\parallel,2}$ direction presented below.

Mattis-Bardeen modeling with field-dependent gap suppression does not describe the data well, even if we assume that the hysteresis is due to misalignment. While $\langle\text{TWPA}\,S_{21}\rangle_{4-8\,\text{GHz}}$ versus T and $B_{\parallel,1}$ appear similar, field-dependent models predict sudden changes only near B_c,

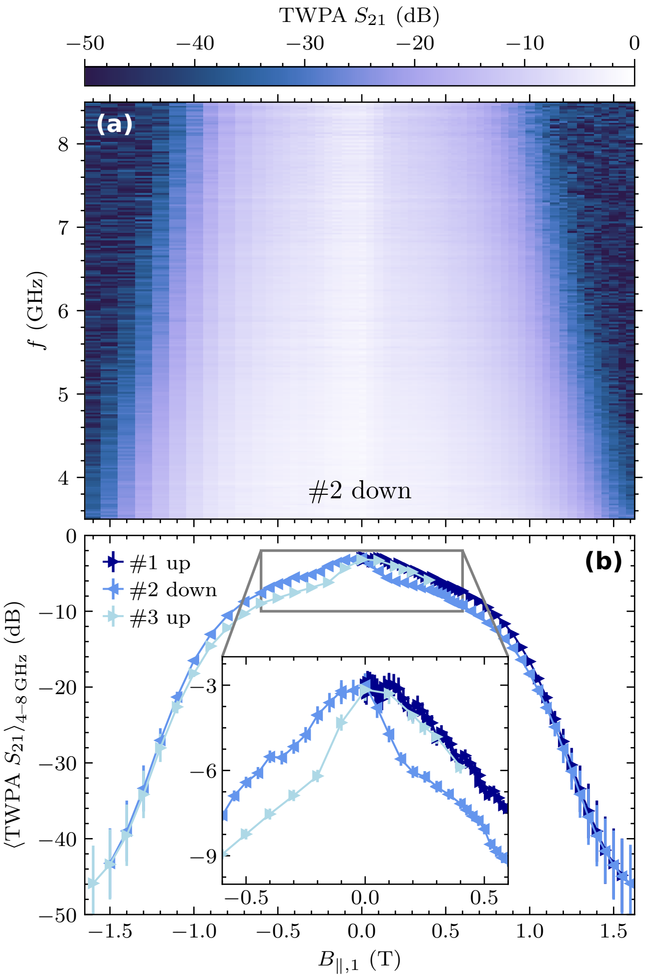

FIG. 8. (a) TWPA S_{21} as a function of $B_{\parallel,1}$ and frequency. (b) Average insertion loss $\langle$TWPA $S_{21}\rangle_{4-8\,\mathrm{GHz}}$ for different sweeps of $B_{\parallel,1}$. The TWPA is initialized by a thermal cycle in zero field. The field is then ramped to 1.6 T, down to −1.6 T, and back up past 0 T. The inset shows the magnified low-field region.

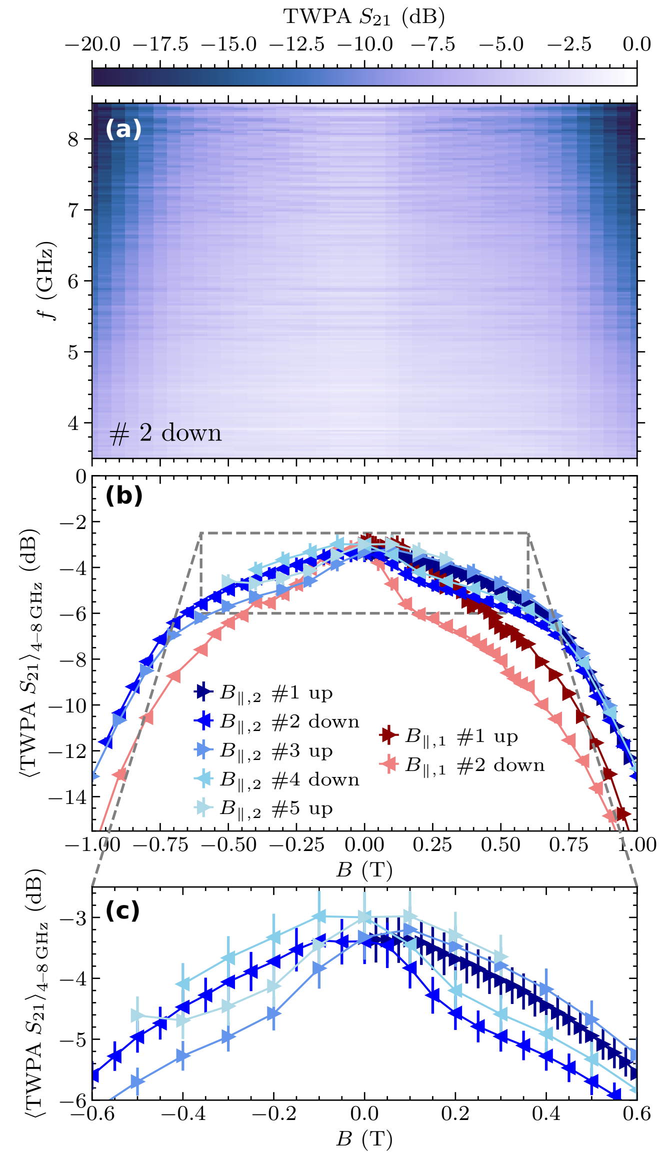

FIG. 9. (a) TWPA S_{21} as a function of $B_{\parallel,2}$ and frequency. (b) $\langle$TWPA $S_{21}\rangle_{4-8\,\mathrm{GHz}}$ as a function of $B_{\parallel,2}$ and $B_{\parallel,1}$ for comparison. Interestingly, the second in-plane direction shows less hysteresis and a slower suppression of $\langle$TWPA $S_{21}\rangle_{4-8\,\mathrm{GHz}}$. The different behavior in the two in-plane directions could be due to alignment or due to device geometry playing a role that we do not understand yet. (c) $\langle$TWPA $S_{21}\rangle_{4-8\,\mathrm{GHz}}$ as a function of $B_{\parallel,2}$ in the low-field region. When the field is swept back and forth with progressively smaller amplitudes toward zero, $\langle$TWPA $S_{21}\rangle_{4-8\,\mathrm{GHz}}$ can be slightly improved. This suggests that, after thermal cycles at nominally zero field, the device likely has some vortex losses.

whereas we observe gradual degradation at much lower fields. Given the likely combination of misalignment-induced vortices, screening currents, and in-plane fields affecting vortex dynamics, we concluded that fitting complex models to the field dependence would not provide additional insight.

2. $B_{\parallel,2}$ direction

For the second in-plane direction, we acquired only transmission data (no gain or ΔSNR measurements). Data are shown in Fig. 9. Vector-magnet limitations restricted the $B_{\parallel,2}$ field range, and the TWPA would not fit into the puck of the fridge with the 6 T axis aligned to the $B_{\parallel,2}$ direction. Thus, measurements focused mainly on the $B_{\parallel,1}$ direction, where the transmission through the TWPA can be fully suppressed with field. To compare the two in-plane field directions, Fig. 9(b) shows mean $\langle$TWPA $S_{21}\rangle_{4-8\,\mathrm{GHz}}$ versus both $B_{\parallel,2}$ and $B_{\parallel,1}$. The field dependence is similar, but $\langle$TWPA $S_{21}\rangle_{4-8\,\mathrm{GHz}}$ suppression is less pronounced and hysteresis is smaller for $B_{\parallel,2}$, possibly indicating better in-plane alignment for that direction. However, the reduced hysteresis could also result from the smaller maximum field before reversing the scan direction. Given the meandering geometry of the TWPA (see Fig. 1), neither the $B_{\parallel,1}$

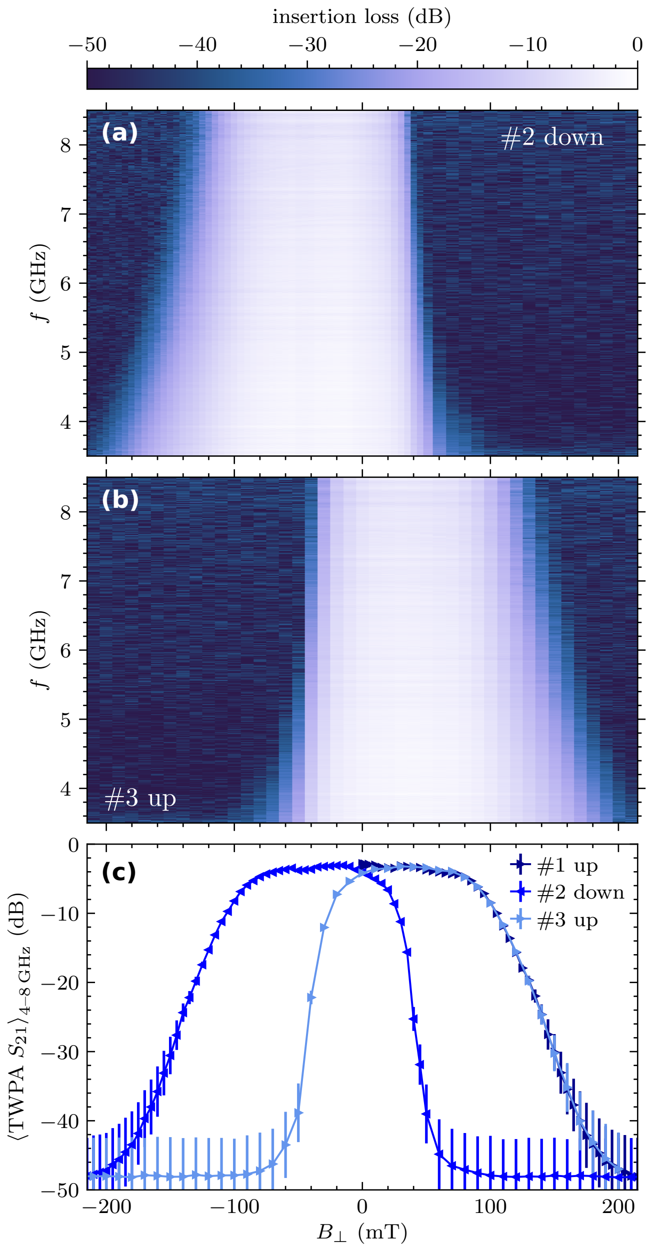

FIG. 10. (a),(b) TWPA S_{21} as a function of $B_\perp$ and frequency for a downward and subsequent upward sweep. Hysteresis is clearly strongest for $B_\perp$, as expected. (c) $\langle \mathrm{TWPA}\, S_{21}\rangle_{4-8\,\mathrm{GHz}}$ for different sweeps of $B_\perp$.

nor the $B_{\parallel,2}$ direction is perfectly aligned with the device current flow, and differences between the field directions are not expected except due to a possible difference in misalignment.

3. $B_\perp$ direction

The $B_\perp$ dependence of the TWPA insertion loss is shown in Fig. 10. Figure 10(b) shows the strong hysteresis of $\langle \mathrm{TWPA}\, S_{21}\rangle_{4-8\,\mathrm{GHz}}$ as a function of $B_\perp$. This hysteresis is similar to that observed in resonators [51]. TWPA transmission is fully suppressed around 200 mT and only starts to recover around 80 mT during the downward sweep, peaking beyond zero field. The initial transmission can be recovered by thermal cycling, which we performed between all separate field sweeps. One could also sweep back and forth with progressively smaller amplitudes to recover the initial transmission [51], as we observed for the $B_{\parallel,2}$ direction in Fig. 9(c).

APPENDIX F: DC CHARACTERIZATION OF MATERIAL T_c AND B_c

To determine T_c and B_c of the materials used in the TWPA, nominally identical Nb and NbTiN films were deposited and measured in a physical property measurement system (PPMS). Four-terminal resistance measurements were acquired as functions of temperature T and magnetic field $B_\perp$. We extract T_c from the midpoint of the superconducting transition [Fig. 11(a)]. The plot of T_c versus $B_\perp$ [Fig. 11(b)] shows a linear decrease with increasing field, similar to other thin-film superconductors [71,72]. We estimate the zero-temperature critical field in two ways. First, using proper extensions of the Abrikosov-Gorkov (AG) theory of T_c suppression by magnetic impurities (see Chapter 10 of Ref. [69]), or equivalently the results of Werthamer-Helfand-Hohenberg (WHH) [73] for weakly coupled BCS superconductors in the dirty limit, the zero-temperature upper critical field can be related to its temperature derivative near T_c:

$$B_{c2}(0) = 0.69 T_c \left[\frac{dB_{c2}}{dT}\right]_{T=T_c}.$$

From a linear fit to the data for Nb, we thus obtain a critical field of 1.34 T; this is slightly smaller than the field of approximately 1.5 T at which we observe full suppression of TWPA S_{21}. This may be due to our assumption of negligible spin-paramagnetic effects and spin-orbit interactions. Moreover, the 0.69 prefactor may not be accurate for niobium films [74].

As an alternative to the linear fit, we fit the data using the AG relationship between T_c and the parameter α characterizing the strength of the relevant pair-breaking mechanism [69], using

$$\ln\left(\frac{T_c}{T_{c0}}\right) = \psi\left(\frac{1}{2}\right) - \psi\left(\frac{1}{2} + \frac{\alpha}{T_c/T_{c0}}\right),$$

where $\psi(x)$ is the digamma function and $T_{c0} = T_c(0)$ is the critical temperature in the absence of pair breaking, $\alpha = 0$. For thin films in perpendicular fields, $\alpha = DeB_\perp/c$, where D is the electronic diffusion constant and $B_\perp$ is the magnetic field [69]. This makes α linearly proportional to the applied field, with the proportionality constant determined

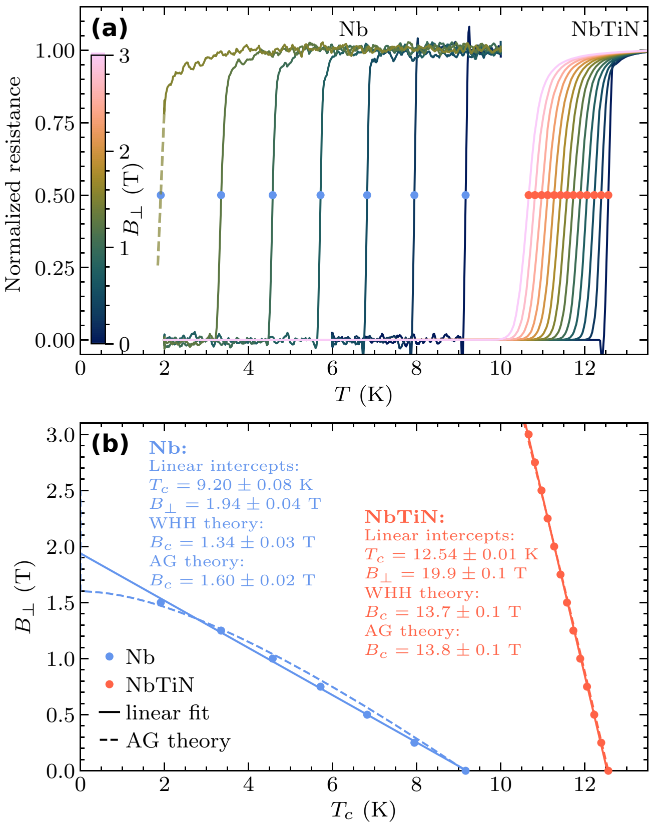

FIG. 11. (a) Normalized resistance as a function of temperature T for Nb and NbTiN films from a similar device at different $B_\perp$. T_c is extracted from the midpoint of the transitions. For $B_\perp = 1.5\,\mathrm{T}$, the highest-field data point for Nb, the transition could not be fully observed because the minimum temperature of the measurement system was 2 K; the data were extrapolated (dashed line) to obtain an estimate. (b) T_c at different B shows a linear decrease with increasing field, consistent with a disordered superconductor. We can estimate B_c and T_c based on the axis intersects of a linear fit for the two superconductors or the AG model described in the text; for NbTiN, the two fits are indistinguishable over the range of the plot.

by material properties. In practice, we write α in the form $\alpha = B_\perp/B_c$ and implement this model numerically, solving the transcendental equation and fitting our experimental data with B_c as the only free parameter while keeping $T_c(0)$ fixed at the measured zero-field value. This approach gives $B_c \simeq 1.6\,\mathrm{T}$, a value in better agreement with the observed suppression of TWPA S_{21}, even though the model does not fit the data as well as the simpler linear fit. Measurements also indicate that the NbTiN critical field is large enough that it will not limit TWPA performance, since the fitted AG value of B_c for NbTiN is approximately 13.8 T (close to the linear-fit intersect multiplied by 0.69). From this critical field value, we estimate the coherence length ξ via the relation $B_c = \phi_0/2\pi\xi^2$, finding $\xi \simeq 4.9\,\mathrm{nm}$.

APPENDIX G: T_c ESTIMATE BASED ON COOLDOWN DATA

We can also estimate critical temperatures of NbTiN and Nb films from S_{21} and S_{22} measurements during TWPA cooldown. We measure S_{22} using the circulator at the TWPA output (Fig. 5). The temperature dependence of TWPA S_{21} [Fig. 12(a)] shows that transmission appears only below 9.15 K, consistent with the T_c of the Nb ground plane (see Appendix F).

Reflection S_{22} [Fig. 12(b)] shows a clear transition around 12.0 K, close to the T_c of the NbTiN microstrip but slightly lower than the dc characterization data on nominally identical films. Full reflection before the NbTiN superconducting transition is consistent with the resistive conducting microstrip representing an

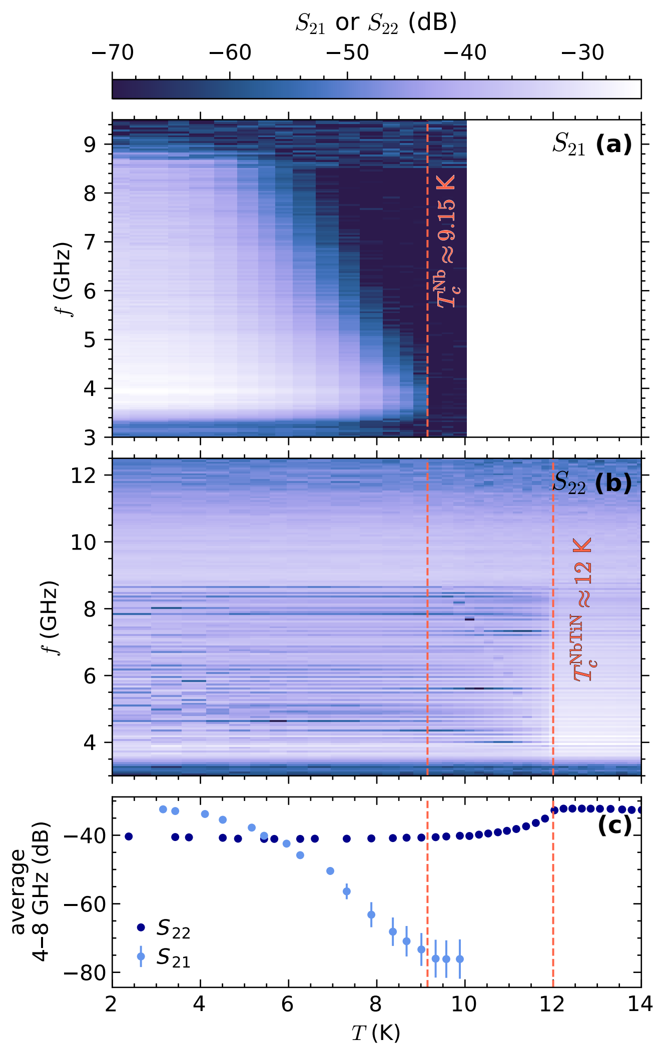

FIG. 12. Transmission S_{21} through (a) and reflection S_{22} from (b) the TWPA. The critical temperatures of the different materials are indicated. Transmission breaks down as the Nb ground plane transitions to its nonsuperconducting state. The reflection data clearly show when the NbTiN microstrip transitions.

extreme impedance mismatch. However, the sudden low-temperature frequency-dependent change in S_{22} around 8.5 GHz results from the diplexer and has nothing to do with the TWPA. Curiously, temperature-dependent photonic bandgap frequency likely appears as a faint reflection peak between 9 and 12 K.

APPENDIX H: FIELD AND TEMPERATURE DEPENDENCE OF THE SETUP TRANSMISSION WITHOUT THE TWPA

The question arises whether setup components have magnetic field or temperature dependence that could be conflated with the TWPA effects. Circulators are natural candidates, as is the superconducting NbTi cable between the mixing chamber and the 4 K stage. Circulators have magnetic shields, but these primarily protect other components from circulator stray fields rather than protecting the circulator from external fields; the shields fail at relatively low fields. HEMT amplifiers could also show magnetic field dependence, but they are mounted far from the magnet center, at the 4 K stage. Stray fields in our setup were previously reported in Ref. [15].

To estimate these effects, we also measured the bypass configuration, where the TWPA was replaced by a short cable, as a function of magnetic field and temperature. The field dependence of the bypass configuration S_{21} is shown in Fig. 13. We chose the z direction because it corresponds to the 6 T field direction of our vector magnet. Measurements differ by a fraction of a decibel from the calibration measurements, which were taken on a different occasion. However, except for frequencies below 4 GHz (the circulator band edge), almost no field dependence is visible. Minimal hysteresis can be observed (we also measured while sweeping the field back down), but overall effects appear negligible, particularly since we exclude data below 4 GHz for TWPA figures of merit.

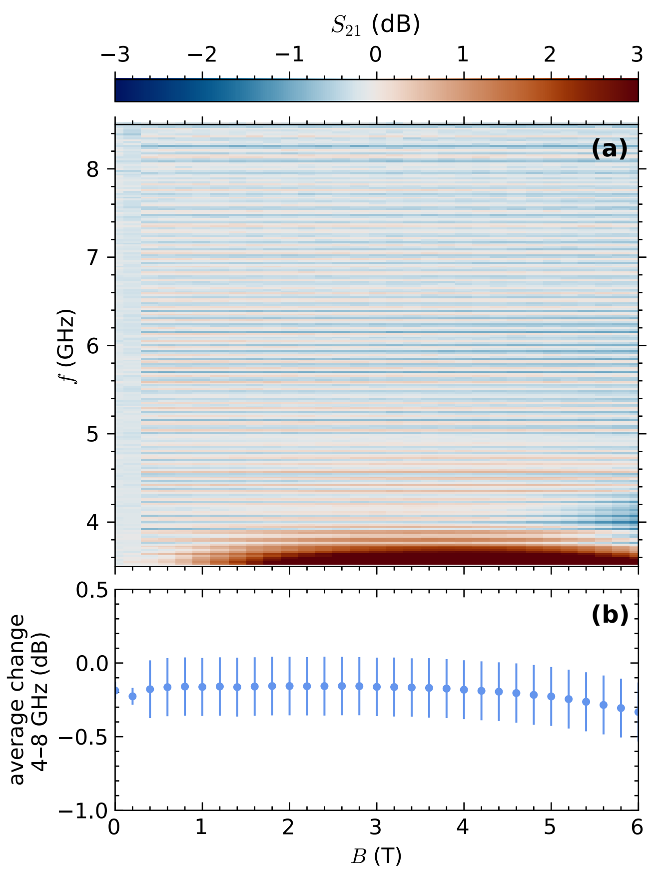

FIG. 13. (a) Change in S_{21} for a bypass cable instead of the TWPA, showing that magnetic field $B_{\parallel,1}$ has little effect on the calibration. At low frequencies, the circulator band edge seems to shift downward at higher field, actually improving transmission. (b) $\langle S_{21}\rangle_{4-8\,\mathrm{GHz}}$ as a function of T compared to the calibration dataset. There is a loss of a fraction of a decibel, but this might have been by a slightly loose cable. At the highest fields, some losses increase.

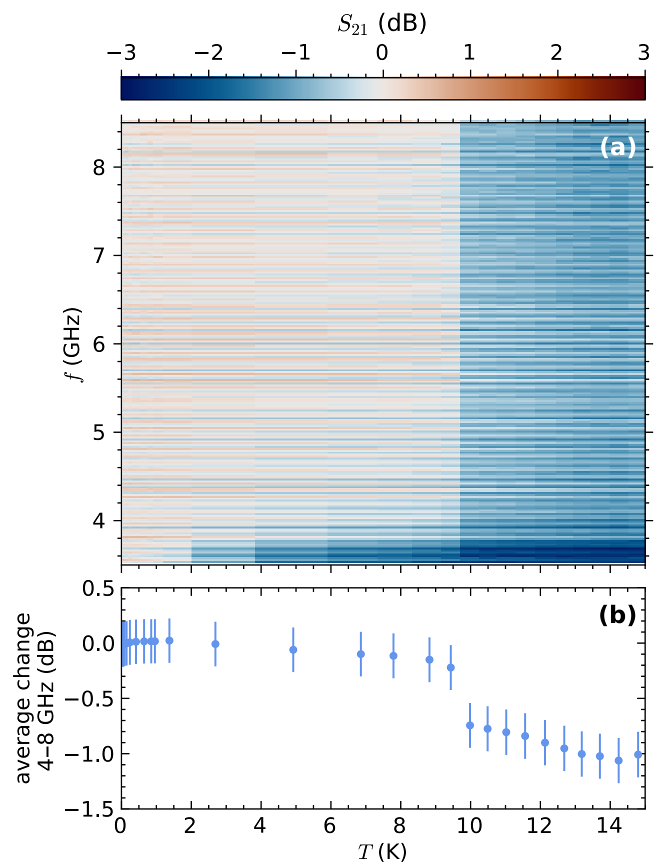

FIG. 14. (a) Change in S_{21} for a bypass cable instead of the TWPA, showing that temperature T does not affect the calibration in the relevant range. (b) $\langle S_{21}\rangle_{4-8\,\mathrm{GHz}}$ as a function of T compared to the calibration dataset. Around 10 K there is a sudden jump, likely due to the transition of the superconducting coaxial cable between the mixing chamber and the HEMT amplifier at the 4 K stage. There is also likely a slight shift in the circulator band edge with T.

The temperature dependence of the bypass configuration S_{21} (Fig. 14) shows weak effects that similarly do not influence TWPA characterization. Small circulator band-edge changes occur around 2 K but only for frequencies below 4 GHz. A jump at 10 K is consistent with the superconducting transition of the NbTi cable between the mixing chamber and the HEMT amplifier at the 4 K stage. At this temperature, the TWPA shows no transmission, so this does not affect TWPA characterization.

[1] B. Ho Eom, P. K. Day, H. G. LeDuc, and J. Zmuidzinas, A wideband, low-noise superconducting amplifier with high dynamic range, Nat. Phys. **8**, 623 (2012).

[2] M. Malnou, M. R. Vissers, J. D. Wheeler, J. Aumentado, J. Hubmayr, J. N. Ullom, and J. Gao, Three-wave mixing kinetic inductance traveling-wave amplifier with near-quantum-limited noise performance, PRX Quantum **2**, 010302 (2021).

[3] F. Faramarzi, R. Stephenson, S. Sypkens, B. H. Eom, H. LeDuc, and P. Day, A 4–8 GHz kinetic inductance traveling-wave parametric amplifier using four-wave mixing with near quantum-limited noise performance, APL Quantum **1**, 036107 (2024).

[4] F. Faramarzi, S. Sypkens, R. Stephenson, B. H. Eom, H. LeDuc, S. Chaudhuri, and P. Day, Near-quantum-limited subgigahertz TiN kinetic inductance traveling-wave parametric amplifier operating in a frequency-translating mode, Phys. Rev. Appl. **23**, 024063 (2025).

[5] L. Howe, A. Giachero, M. Vissers, J. Wheeler, J. Austermann, J. Hubmayr, and J. Ullom, Compact superconducting kinetic inductance traveling wave parametric amplifiers with on-chip rf components, IEEE Trans. Appl. Supercond. **35**, 1 (2025).

[6] C. Bockstiegel, J. Gao, M. R. Vissers, M. Sandberg, S. Chaudhuri, A. Sanders, L. R. Vale, K. D. Irwin, and D. P. Pappas, Development of a broadband NbTiN traveling wave parametric amplifier for MKID readout, J. Low Temp. Phys. **176**, 476 (2014).

[7] N. Zobrist, B. H. Eom, P. Day, B. A. Mazin, S. R. Meeker, B. Bumble, H. G. LeDuc, G. Coiffard, P. Szypryt, N. Fruitwala, I. Lipartito, and C. Bockstiegel, Wide-band parametric amplifier readout and resolution of optical microwave kinetic inductance detectors, Appl. Phys. Lett. **115**, 042601 (2019).

[8] A. Giachero, C. Barone, M. Borghesi, G. Carapella, A. P. Caricato, I. Carusotto, W. Chang, A. Cian, D. Di Gioacchino, E. Enrico, *et al.*, Detector array readout with traveling wave amplifiers, J. Low Temp. Phys. **209**, 658 (2022).

[9] M. A. Castellanos-Beltran, L. Howe, A. Giachero, M. R. Vissers, D. Labranca, J. N. Ullom, and P. F. Hopkins, Measurable improvement in multi-qubit readout using a kinetic inductance traveling wave parametric amplifier, IEEE Trans. Appl. Supercond. **35**, 1 (2025).

[10] C. Macklin, K. O'Brien, D. Hover, M. E. Schwartz, V. Bolkhovsky, X. Zhang, W. D. Oliver, and I. Siddiqi, A near-quantum-limited Josephson traveling-wave parametric amplifier, Science **350**, 307 (2015).

[11] T. C. White, J. Y. Mutus, I.-C. Hoi, R. Barends, B. Campbell, Y. Chen, Z. Chen, B. Chiaro, A. Dunsworth, E. Jeffrey, *et al.*, Traveling wave parametric amplifier with Josephson junctions using minimal resonator phase matching, Appl. Phys. Lett. **106**, 242601 (2015).

[12] L. Planat, A. Ranadive, R. Dassonneville, J. Puertas Martínez, S. Léger, C. Naud, O. Buisson, W. Hasch-Guichard, D. M. Basko, and N. Roch, Photonic-crystal Josephson traveling-wave parametric amplifier, Phys. Rev. X **10**, 021021 (2020).

[13] H. Renberg Nilsson, A. Fadavi Roudsari, D. Shiri, P. Delsing, and V. Shumeiko, High-gain traveling-wave parametric amplifier based on three-wave mixing, Phys. Rev. Appl. **19**, 044056 (2023).

[14] V. Gaydamachenko, C. Kissling, and L. Grünhaupt, rf-SQUID-based traveling-wave parametric amplifier with input saturation power of −84 dbm across more than one octave in bandwidth, Phys. Rev. Appl. **23**, 064053 (2025).

[15] L. M. Janssen, G. Butseraen, J. Krause, A. Coissard, L. Planat, N. Roch, G. Catelani, Y. Ando, and C. Dickel, Magnetic field dependence of a Josephson traveling-wave parametric amplifier and integration into a high-field setup, Phys. Rev. Appl. **22**, 054018 (2024).

[16] M. Khalifa and J. Salfi, Nonlinearity and parametric amplification of superconducting nanowire resonators in magnetic field, Phys. Rev. Appl. **19**, 034024 (2023).

[17] M. Xu, R. Cheng, Y. Wu, G. Liu, and H. X. Tang, Magnetic field-resilient quantum-limited parametric amplifier, PRX Quantum **4**, 010322 (2023).

[18] L. J. Splitthoff, J. J. Wesdorp, M. Pita-Vidal, A. Bargerbos, Y. Liu, and C. K. Andersen, Gate-tunable kinetic inductance parametric amplifier, Phys. Rev. Appl. **21**, 014052 (2024).

[19] N. Zapata, I. Takmakov, S. Günzler, S. Geisert, S. Ihssen, M. Field, A. Nambisan, D. Rieger, T. Reisinger, W. Wernsdorfer, and I. M. Pop, Granular aluminum parametric amplifier for low-noise measurements in tesla fields, Phys. Rev. Lett. **133**, 260604 (2024).

[20] S. Frasca, C. Roy, G. Beaulieu, and P. Scarlino, Three-wave-mixing quantum-limited kinetic inductance parametric amplifier operating at 6 T near 1 K, Phys. Rev. Appl. **21**, 024011 (2024).

[21] A. Vaartjes, A. Kringhøj, W. Vine, T. Day, A. Morello, and J. J. Pla, Strong microwave squeezing above 1 tesla and 1 kelvin, Nat. Commun. **15**, 4229 (2024).

[22] W. Uilhoorn, J. G. Kroll, A. Bargerbos, S. D. Nabi, C.-K. Yang, P. Krogstrup, L. P. Kouwenhoven, A. Kou, and G. de Lange, Quasiparticle trapping by orbital effect in a hybrid superconducting-semiconducting circuit, arXiv:2105.11038.

[23] Z. Wang, L. Balembois, M. Rančić, E. Billaud, M. Le Dantec, A. Ferrier, P. Goldner, S. Bertaina, T. Chanelière, D. Esteve, D. Vion, P. Bertet, and E. Flurin, Single-electron spin resonance detection by microwave photon counting, Nature **619**, 276 (2023).

[24] C. Bartram, T. Braine, R. Cervantes, N. Crisosto, N. Du, G. Leum, P. Mohapatra, T. Nitta, L. J. Rosenberg, G. Rybka, *et al.*, Dark matter axion search using a Josephson traveling wave parametric amplifier, Rev. Sci. Instrum. **94**, 044703 (2023).

[25] R. Di Vora, A. Lombardi, A. Ortolan, R. Pengo, G. Ruoso, C. Braggio, G. Carugno, L. Taffarello, G. Cappelli, N. Crescini, *et al*., Search for galactic axions with a traveling wave parametric amplifier, Phys. Rev. D **108**, 062005 (2023).

[26] V. Elhomsy, L. Planat, D. J. Niegemann, B. Cardoso-Paz, A. Badreldin, B. Klemt, V. Thiney, R. Lethiecq, E. Eyraud, M. C. Dartiailh, B. Bertrand, H. Niebojewski, C. Bäuerle, M. Vinet, T. Meunier, N. Roch, and M. Urdampilleta, Broadband parametric amplification for multiplexed SiMOS quantum dot signals, Phys. Rev. Appl. **24**, 064062 (2025).

[27] Microsoft Azure Quantum, M. Aghaee, A. Alcaraz Ramirez, Z. Alam, R. Ali, M. Andrzejczuk, A. Antipov, M. Astafev, A. Barzegar, B. Bauer, *et al*., Interferometric single-shot parity measurement in InAs–Al hybrid devices, Nature **638**, 651 (2025).

[28] M. Aghaee, Z. Alam, R. Andersen, M. Andrzejczuk, A. Antipov, M. Astafev, L. Avilovas, A. Azizimanesh, B. Bauer, J. Becker, *et al.*, Distinct lifetimes for x and z loop measurements in a Majorana tetron device, arXiv:2507.08795.

[29] F. Luthi, T. Stavenga, O. W. Enzing, A. Bruno, C. Dickel, N. K. Langford, M. A. Rol, T. S. Jespersen, J. Nygård, P. Krogstrup, and L. DiCarlo, Evolution of nanowire transmon qubits and their coherence in a magnetic field, Phys. Rev. Lett. **120**, 100502 (2018).

[30] A. Schneider, T. Wolz, M. Pfirrmann, M. Spiecker, H. Rotzinger, A. V. Ustinov, and M. Weides, Transmon qubit in a magnetic field: Evolution of coherence and transition frequency, Phys. Rev. Res. **1**, 023003 (2019).

[31] M. Pita-Vidal, A. Bargerbos, C.-K. Yang, D. J. van Woerkom, W. Pfaff, N. Haider, P. Krogstrup, L. P. Kouwenhoven, G. de Lange, and A. Kou, Gate-tunable field-compatible fluxonium, Phys. Rev. Appl. **14**, 064038 (2020).

[32] A. Kringhøj, T. W. Larsen, O. Erlandsson, W. Uilhoorn, J. G. Kroll, M. Hesselberg, R. P. G. McNeil, P. Krogstrup, L. Casparis, C. M. Marcus, and K. D. Petersson, Magnetic-field-compatible superconducting transmon qubit, Phys. Rev. Appl. **15**, 054001 (2021).

[33] J. Krause, C. Dickel, E. Vaal, M. Vielmetter, J. Feng, R. Bounds, G. Catelani, J. M. Fink, and Y. Ando, Magnetic field resilience of three-dimensional transmons with thin-film Al/AlO_x/Al Josephson junctions approaching 1 T, Phys. Rev. Appl. **17**, 034032 (2022).

[34] J. Krause, G. Marchegiani, L. Janssen, G. Catelani, Y. Ando, and C. Dickel, Quasiparticle effects in magnetic-field-resilient three-dimensional transmons, Phys. Rev. Appl. **22**, 044063 (2024).

[35] S. Günzler, J. Beck, D. Rieger, N. Gosling, N. Zapata, M. Field, S. Geisert, A. Bacher, J. K. Hohmann, M. Spiecker, *et al.*, Spin environment of a superconducting qubit in high magnetic fields, Nat. Commun. **16**, 9564 (2025).

[36] G. Zheng, N. Samkharadze, M. L. Noordam, N. Kalhor, D. Brousse, A. Sammak, G. Scappucci, and L. M. K. Vandersypen, Rapid gate-based spin read-out in silicon using an on-chip resonator, Nat. Nanotechnol. **14**, 742 (2019).

[37] S. Schaal, I. Ahmed, J. A. Haigh, L. Hutin, B. Bertrand, S. Barraud, M. Vinet, C.-M. Lee, N. Stelmashenko, J. W. A. Robinson, J. Y. Qiu, S. Hacohen-Gourgy, I. Siddiqi, M. F. Gonzalez-Zalba, and J. J. L. Morton, Fast gate-based readout of silicon quantum dots using Josephson parametric amplification, Phys. Rev. Lett. **124**, 067701 (2020).

[38] D. de Jong, C. G. Prosko, D. M. A. Waardenburg, L. Han, F. K. Malinowski, P. Krogstrup, L. P. Kouwenhoven, J. V. Koski, and W. Pfaff, Rapid microwave-only characterization and readout of quantum dots using multiplexed gigahertz-frequency resonators, Phys. Rev. Appl. **16**, 014007 (2021).

[39] A. Bienfait, J. J. Pla, Y. Kubo, M. Stern, X. Zhou, C. C. Lo, C. D. Weis, T. Schenkel, M. L. W. Thewalt, D. Vion, D. Esteve, B. Julsgaard, K. Mølmer, J. J. L. Morton, and P. Bertet, Reaching the quantum limit of sensitivity in electron spin resonance, Nat. Nanotechnol. **11**, 253 (2016).

[40] W. Vine, M. Savytskyi, A. Vaartjes, A. Kringhøj, D. Parker, J. Slack-Smith, T. Schenkel, K. Mølmer, J. C. McCallum, B. C. Johnson, A. Morello, and J. J. Pla, In situ amplification of spin echoes within a kinetic inductance parametric amplifier, Sci. Adv. **9**, eadg1593 (2023).

[41] M. Kounalakis, Y. M. Blanter, and G. A. Steele, Flux-mediated optomechanics with a transmon qubit in the single-photon ultrastrong-coupling regime, Phys. Rev. Res. **2**, 023335 (2020).

[42] T. Bera, S. Majumder, S. K. Sahu, and V. Singh, Large flux-mediated coupling in hybrid electromechanical system with a transmon qubit, Commun. Phys. **4**, 12 (2021).

[43] Y. Tabuchi, S. Ishino, A. Noguchi, T. Ishikawa, R. Yamazaki, K. Usami, and Y. Nakamura, Coherent coupling between a ferromagnetic magnon and a superconducting qubit, Science **349**, 405 (2015).

[44] M. Kounalakis, G. E. W. Bauer, and Y. M. Blanter, Analog quantum control of magnonic cat states on a chip by a superconducting qubit, Phys. Rev. Lett. **129**, 037205 (2022).

[45] S. Chaudhuri, Introducing the Princeton Axion Search (PXS), in *APS April Meeting Abstracts*, APS Meeting Abstracts (American Physical Society, 2024), Vol. 2024, p. J14.005.

[46] K. Ramanathan, N. Klimovich, R. Basu Thakur, B. H. Eom, H. G. Leduc, S. Shu, A. D. Beyer, and P. K. Day, Wideband direct detection constraints on hidden photon dark matter with the qualiphide experiment, Phys. Rev. Lett. **130**, 231001 (2023).

[47] M. Malnou, J. Aumentado, M. R. Vissers, J. D. Wheeler, J. Hubmayr, J. N. Ullom, and J. Gao, Performance of a kinetic inductance traveling-wave parametric amplifier at 4 kelvin: Toward an alternative to semiconductor amplifiers, Phys. Rev. Appl. **17**, 044009 (2022).

[48] D. C. Mattis and J. Bardeen, Theory of the anomalous skin effect in normal and superconducting metals, Phys. Rev. **111**, 412 (1958).

[49] H. T. Friis, A note on a simple transmission formula, Proc. IRE **34**, 254 (1946).

[50] S. Kwon, A. Fadavi Roudsari, O. W. B. Benningshof, Y.-C. Tang, H. R. Mohebbi, I. A. J. Taminiau, D. Langenberg, S. Lee, G. Nichols, D. G. Cory, and G.-X. Miao, Magnetic field dependent microwave losses in superconducting niobium microstrip resonators, J. Appl. Phys. **124**, 033903 (2018).

[51] D. Bothner, T. Gaber, M. Kemmler, D. Koelle, R. Kleiner, S. Wünsch, and M. Siegel, Magnetic hysteresis effects in superconducting coplanar microwave resonators, Phys. Rev. B **86**, 014517 (2012).

[52] L. Nulens, N. Lejeune, J. Caeyers, S. Marinković, I. Cools, H. Dausy, S. Basov, B. Raes, M. J. Van Bael, A. Geresdi, A. V. Silhanek, and J. Van de Vondel, Catastrophic magnetic flux avalanches in NbTiN superconducting resonators, Commun. Phys. **6**, 267 (2023).

[53] C. Song, T. W. Heitmann, M. P. DeFeo, K. Yu, R. McDermott, M. Neeley, J. M. Martinis, and B. L. T. Plourde, Microwave response of vortices in superconducting thin films of Re and Al, Phys. Rev. B **79**, 174512 (2009).

[54] D. Bothner, T. Gaber, M. Kemmler, D. Koelle, and R. Kleiner, Improving the performance of superconducting microwave resonators in magnetic fields, Appl. Phys. Lett. **98**, 102504 (2011).

[55] J. G. Kroll, F. Borsoi, K. L. van der Enden, W. Uilhoorn, D. de Jong, M. Quintero-Pérez, D. J. van Woerkom, A. Bruno, S. R. Plissard, D. Car, E. P. A. M. Bakkers, M. C. Cassidy, and L. P. Kouwenhoven, Magnetic-field-resilient superconducting coplanar-waveguide resonators for hybrid circuit quantum electrodynamics experiments, Phys. Rev. Appl. **11**, 064053 (2019).

[56] N. Samkharadze, A. Bruno, P. Scarlino, G. Zheng, D. P. DiVincenzo, L. DiCarlo, and L. M. K. Vandersypen, High-kinetic inductance superconducting nanowire resonators for circuit QED in a magnetic field, Phys. Rev. Appl. **5**, 044004 (2016).

[57] L. M. Janssen, F. Faramarzi, H. G. LeDuc, S. Patel, G. Catelani, P. K. Day, Y. Ando, and C. Dickel, Data and code for "Magnetic-field and temperature limits of a kinetic-inductance traveling-wave parametric amplifier" (2025), doi:10.5281/zenodo.17148287

[58] J. H. Nielsen *et al.*, Qcodes/qcodes: Qcodes 0.43.0, 2024, doi:10.5281/zenodo.10459033

[59] M. A. Rol, C. Attryde, J. C. van Oven, K. Loh, J. Gloudemans, V. Negîrneac, T. Last, and C. C. Bultink, Quantify: An open-source framework for operating quantum computers in the NISQ era, in *APS March Meeting Abstracts* (2021), Vol. 2021, pp. M34–001.

[60] S. Shu, N. Klimovich, B. H. Eom, A. D. Beyer, R. B. Thakur, H. G. Leduc, and P. K. Day, Nonlinearity and wide-band parametric amplification in a (Nb,Ti)N microstrip transmission line, Phys. Rev. Res. **3**, 023184 (2021).

[61] J. A. Nelder, R. Mead, and A simplex method for function minimization, A simplex method for function minimization, Comput. J. **7**, 308 (1965).

[62] J. Gao, M. Daal, A. Vayonakis, S. Kumar, J. Zmuidzinas, B. Sadoulet, B. A. Mazin, P. K. Day, and H. G. Leduc, Experimental evidence for a surface distribution of two-level systems in superconducting lithographed microwave resonators, Appl. Phys. Lett. **92**, 152505 (2008).

[63] B. Abdisatarov, D. Bafia, A. Murthy, G. Eremeev, H. E. Elsayed-Ali, J. Lee, A. Netepenko, C. P. A. Carlos, S. Leith, G. J. Rosaz, A. Romanenko, and A. Grassellino, Direct measurement of microwave loss in Nb films for superconducting qubits, Appl. Phys. Lett. **125**, 124002 (2024).

[64] N. Klimovich, S. Wood, P. K. Day, and B.-K. Tan, Investigating the effects of sum-frequency conversions and surface impedance uniformity in traveling wave superconducting parametric amplifiers, J. Appl. Phys. **135**, 124402 (2024).

[65] M. W. Coffey and J. R. Clem, Unified theory of effects of vortex pinning and flux creep upon the rf surface impedance of type-II superconductors, Phys. Rev. Lett. **67**, 386 (1991).

[66] T. Hong, K. Choi, K. I. Sim, T. Ha, B. C. Park, H. Yamamori, and J. H. Kim, Terahertz electrodynamics and superconducting energy gap of NbTiN, J. Appl. Phys. **114**, 243905 (2013).

[67] F. Khan, A. V. Khudchenko, A. M. Chekushkin, and V. P. Koshelets, Characterization of the parameters of superconducting NbN and NbTiN films using parallel plate resonator, IEEE Trans. Appl. Supercond. **32**, 1 (2022).

[68] F. Gross, B. S. Chandrasekhar, D. Einzel, K. Andres, P. J. Hirschfeld, H. R. Ott, J. Beuers, Z. Fisk, and J. L. Smith, Anomalous temperature dependence of the magnetic field penetration depth in superconducting UBe_{13}, Z. Phys. B: Condens. Matter **64**, 175 (1986).

[69] M. Tinkham, *Introduction to Superconductivity* (Dover Publications, Mineola, NY, 2004), 2nd ed.

[70] E. Hammerstad and O. Jensen, Accurate models for microstrip computer-aided design, in *IEEE MTT-S International Microwave Symposium Digest* (IEEE, 1980), pp. 407–409.

[71] A. Semenov, B. Günther, U. Böttger, H.-W. Hübers, H. Bartolf, A. Engel, A. Schilling, K. Ilin, M. Siegel, R. Schneider, D. Gerthsen, and N. A. Gippius, Optical and transport properties of ultrathin NbN films and nanostructures, Phys. Rev. B **80**, 054510 (2009).

[72] X. Zhang, A. Engel, Q. Wang, A. Schilling, A. Semenov, M. Sidorova, H.-W. Hübers, I. Charaev, K. Ilin, and M. Siegel, Characteristics of superconducting tungsten silicide $w_x Si_{1-x}$ for single photon detection, Phys. Rev. B **94**, 174509 (2016).

[73] N. R. Werthamer, E. Helfand, and P. C. Hohenberg, Temperature and purity dependence of the superconducting critical field, H_{c2}. III. Electron spin and spin-orbit effects, Phys. Rev. **147**, 295 (1966).

[74] I. Zaytseva, A. Abaloszew, B. C. Camargo, Y. Syryanyy, and M. Z. Cieplak, Upper critical field and superconductor–metal transition in ultrathin niobium films, Sci. Rep. **10**, 19062 (2020).